


Identifying key stages of radiation fog evolution using water vapor isotopes

Journal Article

Author(s):

Li, Yafei; Eugster, Werner ; Riedl, Andreas ; Westerhuis, Stephanie ; Buchmann, Nina ; Scholder-Aemisegger, Franziska

Publication date:

2023-05-01

Permanent link:

<https://doi.org/10.3929/ethz-b-000605701>

Rights / license:

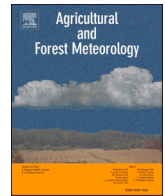
[Creative Commons Attribution 4.0 International](#)

Originally published in:

Agricultural and Forest Meteorology 334, <https://doi.org/10.1016/j.agrformet.2023.109430>

Funding acknowledgement:

175733 - The importance of fog and dew for Swiss grasslands today and in the future (Acronym: IFDewS) (SNF)



Identifying key stages of radiation fog evolution using water vapor isotopes

Yafei Li^{a,*}, Werner Eugster^a, Andreas Riedl^a, Stephanie Westerhuis^{b,c}, Nina Buchmann^a, Franziska Scholder-Aemisegger^d

^a Institute of Agricultural Sciences, ETH Zurich, Zurich, Switzerland

^b Center for Climate Systems Modeling, ETH Zurich, Zurich, Switzerland

^c Federal Office of Meteorology and Climatology, MeteoSwiss, Zurich, Switzerland

^d Institute for Atmospheric and Climate Science, ETH Zurich, Zurich, Switzerland

ARTICLE INFO

Keywords:

Radiation fog evolution
Condensation
Entrainment
Evaporation
Water vapor isotopes
Cold frontal clouds

ABSTRACT

Fog is tied to surface energy and water budgets. However, our knowledge about the processes leading to fog evolution is still fragmentary, and their adequate representation in numerical-weather-prediction and climate models remains challenging. Water vapor isotopes are widely used to investigate Earth's water cycle dynamics and can provide process-based insights into fog evolution. Although isotopes of water vapor and droplets during radiation fog have been reported, the intra-event isotope dynamics and the mechanisms controlling water vapor isotope variability during radiation fog evolution have hardly been investigated. We use water vapor isotopes ($\delta^2\text{H}_v$, d_v) combined with meteorological and eddy-covariance measurements, plus vertical profiles from a high-resolution numerical-weather-prediction model (COSMO-1), to study the processes that influence radiation fog evolution. Variability in surface-humidity and water vapor isotopes is tied to the different stages (shallow, transitional, and deep fog) of radiation fog evolution and affected by condensation, turbulent entrainment, fog droplet deposition at the surface, and evaporation processes. Strong water vapor isotopic fluctuations during radiation fog are linked to fog lifting to stratus-clouds during nighttime that lead to fog dissipation at ground level. Our results reveal highly correlated atmospheric-specific-humidity (q_a) and water vapor isotopes during dew formation which is typical before the onset of radiation fog and in combination with fog; whilst during fog periods, $\delta^2\text{H}_v$ and d_v show larger temporal variability than q_a due to their sensitivity to fog dynamics. Particularly, during fog growth, entrainment of air from the fog-top caused increasing d_v , which was otherwise constant during condensation. Furthermore, $\delta^2\text{H}_v$ variability during the transition into deep fog likely indicated the alternation of condensation-induced-decrease and entrainment-induced-increase of $\delta^2\text{H}_v$. Compared to the temporal isotope variability (with a magnitude of 34.6‰ for $\delta^2\text{H}_v$) associated with large-scale cold-frontal-clouds, radiation fog evolution is found to be associated with isotope variability of a similar amplitude (24.6‰ for $\delta^2\text{H}_v$).

1. Introduction

Fog is an important meteorological phenomenon with atmospheric water input into ecosystems (Dawson, 1998), but is also associated with its negative impact on society and natural environment affecting transportation systems and air quality (Bruijnzeel et al., 2006; LaDochy and Witiw, 2013). Effective measures to address low visibility conditions and deteriorating air quality require accurate fog forecasts. Despite advances in recent years, it is still a challenge to precisely predict fog using numerical weather models (Castillo-Botón et al., 2022; Román-Cascón et al., 2019; Westerhuis, 2020). Uncertainties originate

in the inherently uncertain microphysics (Román-Cascón et al., 2019) and turbulence parametrizations in numerical models (Pithani et al., 2019), coarse vertical (Philip et al., 2016) and horizontal (Boutle et al., 2016) resolutions, and complexity of the terrains (Müller et al., 2010).

Among different types of fog that are categorized by the mechanisms of their formations (e.g., radiation fog and advection fog), radiation fog driven by radiative cooling is common in areas where cold air can sink to ground level on clear and calm nights (Eugster, 2008; Smith et al., 2018). Smith et al. (2018) classified radiation fog into three stages, i.e., shallow fog, fog transition, and deep fog. During shallow radiation fog with depths of 1 m to 10 m (Smith et al., 2018; Stull, 1988), the surface is

* Correspondence author.

E-mail addresses: yafei.li@usys.ethz.ch, l.yafei@outlook.com (Y. Li).

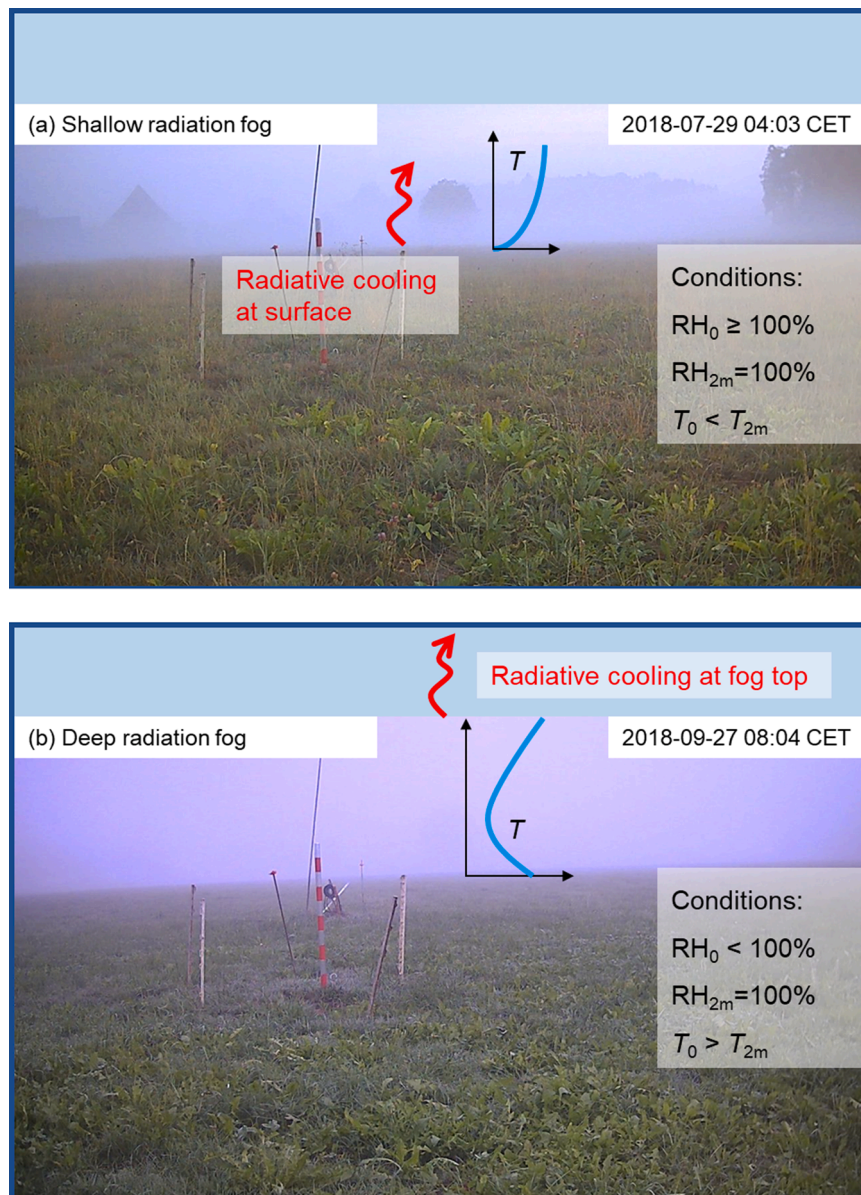


Fig. 1. Schematics and photos of (a) shallow radiation fog, and (b) deep radiation fog at the grassland site Chamau (CH-CHA). The schematics of temperature profile (T) and radiative cooling were adapted from [Smith et al. \(2018\)](#). RH_{2m} is relative humidity measured at 2 m a.g.l.; T_{2m} is air temperature measured at 2 m a.g.l.; RH_0 is normalized surface relative humidity for quantifying the transport potential of water vapor from atmosphere onto the surface at surface temperature (T_0).

the primary location for radiative cooling, and condensation occurs in the near-surface atmosphere when the surface cools below the dew-point temperature of the air ([Fig. 1a](#)). When fog becomes optically thick (up to 100 m), i.e., opaque to thermal radiation in the wavelength range of 8–12 μm , the fog-top becomes the primary region of radiative cooling. Fog-top cooling produces negatively buoyant air that eventually sinks towards the surface ([Smith et al., 2018](#)). Consequently, the newly formed fog layer prohibits surface cooling in the further evolution of the fog event. This induces the development of a saturated well-mixed (i.e., moist-adiabatic) temperature profile at the bottom of the atmospheric boundary layer ([Smith et al., 2018](#)). With the surface being generally warmer than the overlying atmospheric air in such a situation, surface sensible heat fluxes contribute to the development of a deep radiation fog layer ([Fig. 1b](#)). Half of the radiation fog events in Central England have been found to successfully transition from shallow to deep fog, and this transition process takes on average 2 h ([Price, 2011](#)). Shallow radiation fog tends to dissipate shortly after sunrise, whilst deep radiation fog can persist longer ([Price, 2011](#)).

Since the IPCC AR5 report, there has been increasing recognition of the need to better understand the role of land-atmosphere coupling and related feedbacks ([Allan et al., 2021](#)). The evolution of radiation fog is tightly associated with surface-atmosphere interactions. Before fog develops, dew formation deposits water vapor from the near-surface air mass to the ecosystem surfaces ([Price et al., 2018](#)). Heat released by condensation during dew formation can warm up the surface and interrupt the formation of fog ([Price et al., 2018](#)). If fog forms, deposition of fog droplets from the fog layer to the surface can induce fog erosion ([Beswick et al., 1991](#); [Mazoyer et al., 2017](#); [Price and Clark, 2014](#)). Additionally, overlying clouds strongly reduce radiative cooling and can induce fog dissipation during the night; this effect is more significant in cases with low-level clouds, due to enhanced downward longwave warming ([Guo et al., 2021](#); [Waersted et al., 2017](#)). Clouds forming at middle and high levels may prolong the fog lifetime after sunrise, because the overlying clouds (and partly the deep fog layer itself) can increase the reflection of solar radiation and consequently weaken the surface heating from solar radiation ([Guo et al., 2021](#)).

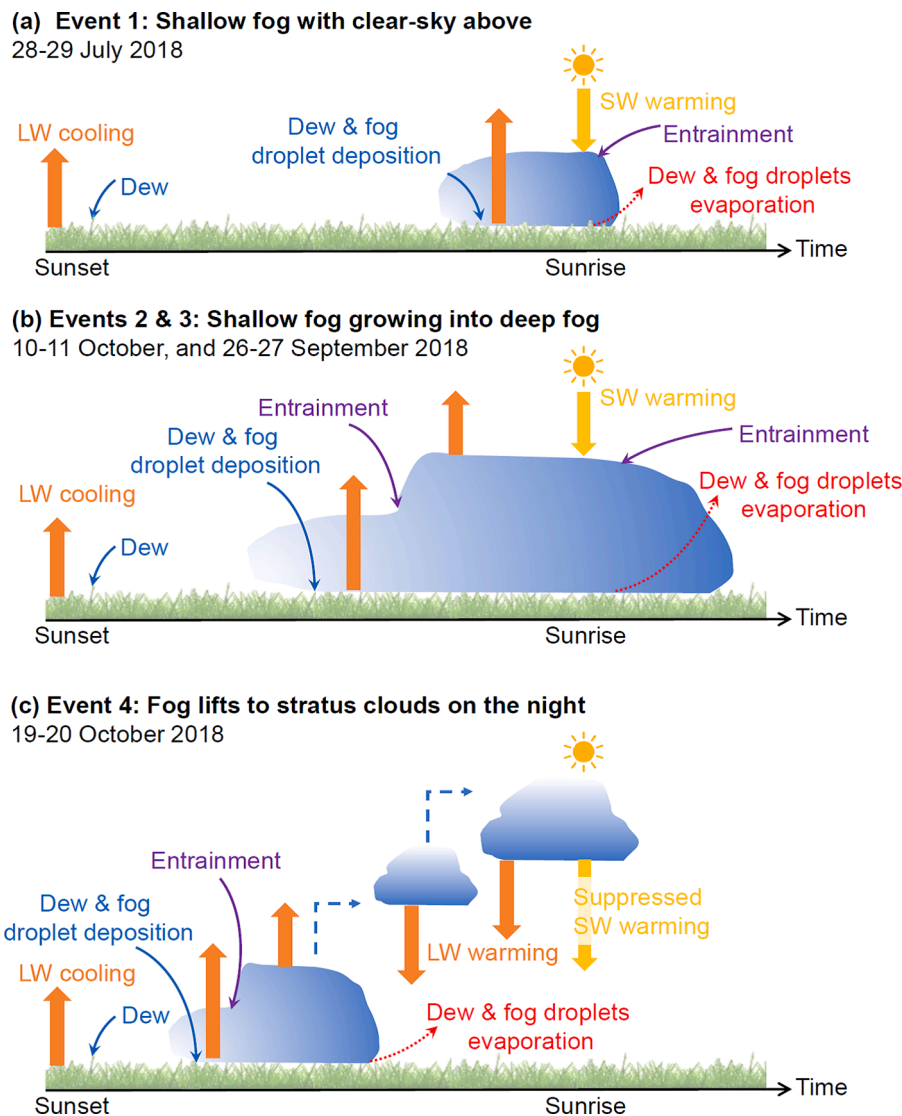


Fig. 2. Schematics of fog evolution during four fog events. LW, longwave radiation. SW, shortwave radiation. Entrainment: entrainment of air from overlaying atmosphere into the fog layer.

As compared to traditional meteorological variables (e.g. specific humidity) in the near-surface atmosphere, stable water isotopes are more sensitive to the different processes affecting the fog's dynamics, and have been used in the past to investigate the sources and formation mechanisms of fog (Fischer et al., 2016; Kaseke and Wang, 2022; Kaseke et al., 2017; Spiegel et al., 2012). The retrieval of $^1\text{H}^2\text{H}^{16}\text{O}$ in atmospheric water vapor supported by satellite-based remote sensing (Lacour et al., 2017; Diekmann et al. 2021; Schneider et al. 2022), allows to assimilate water isotopes into general circulation models, which may potentially improve weather prediction (Tada et al., 2021; Toride et al., 2021), and local uncertainties of reconstructing paleo-climate through a better process-understanding (Breil et al., 2021). The most important isotopologues of water in the hydrological cycle are major and lighter isotopologue $^1\text{H}_2^{16}\text{O}$, as well as minor and heavier isotopologues $^1\text{H}^2\text{H}^{16}\text{O}$ and $^1\text{H}_2^{18}\text{O}$. The isotopic composition of hydrogen or oxygen in water is expressed in the delta notation $\delta = (R_{\text{sample}}/R_{\text{standard}} - 1)$ reported in per mil (‰), where R_{standard} and R_{sample} are the molar ratios of either $^2\text{H}/^1\text{H}$ or $^{18}\text{O}/^{16}\text{O}$ for the standard (Vienna Standard Mean Ocean Water, V-SMOW) and the sample, respectively (IAEA, 2009). With this definition, $\delta^{18}\text{O}$ and $\delta^2\text{H}$ of samples are expressed as ‰ deviations from the standards. Dew and fog formation affect the near-surface atmosphere and land surface moisture budgets, and are associated with phase

changes (i.e., condensation and evaporation processes). During these phase changes, due to the lower saturation vapor pressure, heavier isotopologues will be enriched in liquid phase but depleted in gaseous phase, leading to $\delta^{18}\text{O}$ and $\delta^2\text{H}$ being higher in the liquid phase and lower in the gaseous phase. These changes in isotopic composition are termed isotopic fractionation (Criss, 1999; Merlivat and Jouzel, 1979; Urey, 1947). There are two kinds of isotopic fractionation related to dew and fog processes: (1) Dew and fog formation in saturated atmospheric conditions are dominated by equilibrium-fractionation, with the variability of $\delta^{18}\text{O}$ and $\delta^2\text{H}$ following a 1:8 ratio derived from different saturation vapor pressure of the two isotopologues (Dansgaard, 1964). Previous research found that radiation fog processes are mainly associated with equilibrium-fractionation (Delattre et al., 2015; Kaseke et al., 2017; Li et al., 2021), which most likely refer to shallow radiation fog events with limited dew deposition and supersaturation with respect to the surface. In this study, we show that non-equilibrium conditions can occur in some stages during the evolution of the studied fog events and can complicate isotope variability through non-equilibrium fractionation effects and mixing processes. (2) With dew formation in unsaturated atmospheric conditions, a near-surface humidity gradient (reflected in the relative humidity with respect to surface temperature) induces net removal of water molecules from the liquid-vapor interface,

hence the faster diffusion of $^1\text{H}^2\text{H}^{16}\text{O}$ than $^1\text{H}_2^{18}\text{O}$ leads to the additional changes in $\delta^{18}\text{O}$ and $\delta^2\text{H}$ deviating from the 1:8 ratio, which is termed non-equilibrium fractionation. Therefore, the secondary variable deuterium excess ($d = \delta^2\text{H} - 8\delta^{18}\text{O}$), which does not change during equilibrium fractionation with the changes of $\delta^{18}\text{O}$ and $\delta^2\text{H}$ by 1:8 ratio, is defined to quantify non-equilibrium fractionation.

Different processes affect the isotopic variability of atmospheric water vapor, which is the main source of radiation fog water. Entrainment of water vapor (i.e., through the mixing of environmental air into the fog layer) from the air above the fog layer usually leads to an increase in water vapor d in the near-surface atmosphere (Parkes et al., 2017). This is mainly because the free tropospheric water vapor reservoir (1) has in general a different origin than the boundary layer water vapor; (2) is associated with a longer residence time in the atmosphere; and (3) has a larger probability of having formed clouds and precipitation during transport. Depending on the share of soil evaporation and plant transpiration (Aemisegger et al., 2014), local evapotranspiration can lower d in the near-surface atmosphere (Parkes et al., 2017) when compared to local precipitation, which is the primary source of local evaporation. Elevated water vapor d was observed during cold frontal passages (Spiegel et al., 2012), which could be explained by the water vapor originating from evaporation sites with low relative humidity. Cold frontal passages induced decreasing $\delta^2\text{H}$ in the atmospheric water vapor, whilst $\delta^2\text{H}$ slowly recovered after cold fronts (Aemisegger et al., 2015; Spiegel et al., 2012; Wen et al., 2008). In contrast, increasing $\delta^2\text{H}$ was observed during warm frontal passages (Spiegel et al., 2012; White and Gedzelman, 1984). These signals result from a combination of large-scale warm and cold advection associated with these systems and the local fluxes triggered by the advection of these air masses over a relatively colder or warmer surface (Thurnherr et al. 2021).

With respect to the $\delta^2\text{H}$ - $\delta^{18}\text{O}$ regressions for local precipitation (i.e., local meteoric water line, LMWL), radiation fog water is found to be generally enriched in heavy isotopologues, because i) radiation fog often condenses from local vapor whilst precipitation forms at higher levels in the troposphere (Scholl et al., 2011); and ii) due to their suspended nature, fog droplets are generally exposed to enhanced evaporative enrichment. Furthermore, advective fog events are found to have higher d in fog water compared to radiation fog and local precipitation (Kaseke et al., 2017). However, the intra-event water vapor isotopic dynamics associated with the formation, growth and dissipation of radiation fog have never been investigated to the best of our knowledge. A full life cycle of radiation fog includes temperature and humidity changes at both the surface and in the near-surface atmosphere, which can induce water vapor isotopic variability.

In this study, we investigate the intra-event variability of water vapor isotopes to obtain valuable insights into the land-atmosphere water exchange relevant for radiation fog formation, growth, and dissipation. Our study is based on the following event analyses (Fig. 2): (1) Event 1 was a shallow radiation fog event occurring and dissipating around sunrise. (2 & 3) Event 2 and event 3 were radiation fog events transitioning from shallow to deep fog and persisting longer after sunrise; the difference between the two events is the dominance of condensation vs. fog-top entrainment during fog transition. (4) Event 4 started as a shallow radiation fog and consequently lifted into stratus clouds during the night. (5) Event 5 had no fog with cold frontal clouds.

With these event-based analyses, we provide a systematic interpretation of the water vapor isotopic signal in the near-surface atmosphere over a wide spectrum of conditions affecting fog evolution.

2. Materials and methods

2.1. Study site

The Chamau site (CH-CHA; 47°12'36.8" N, 8°24'37.6" E) is a temperate grassland at 393 m a.s.l. located on the bottom of a broad (16 km wide) valley in Switzerland. Instruments for the long-term eddy

covariance (EC) measurements since 2005 consist of a three-dimensional ultrasonic anemometer-thermometer (model R3-50, Gill Instruments, Lymington, UK) and an open-path infrared gas analyzer (IRGA, Li-7500, Li-Cor, Lincoln, NB, USA). The EC setup is at 2.4 m a.g.l. The EC measurements recorded at 20 Hz were processed to 30 min averages for dew-point temperature (T_{dew} in °C), sensible heat flux (H in W m^{-2}), latent heat flux (LE), horizontal wind speed ($u_{2\text{m}}$ in m s^{-1}) and friction velocity (u^* in m s^{-1}) using EddyPro Version 7.0.6 (LI-COR, 2019) following established community guidelines (Aubinet et al., 2012). Ground heat flux (G in W m^{-2}) was measured at 0.02 m depth with two heat flux plates (HFPO1 heat flux sensor, Hukseflux, Delft, the Netherlands).

Ancillary meteorological instruments were installed at 2.0 m a.g.l. Measurements were taken every 10 s and then aggregated to 30 min averages for air temperature ($T_{2\text{m}}$, in °C), relative humidity ($\text{RH}_{2\text{m}}$ in %) (a shaded, sheltered and ventilated HydroClip HC2A-S3, Rotronic AG, Basserdorf, Switzerland), as well as long-wave and short-wave outgoing and incoming radiation (LW_{out} , LW_{in} , SW_{out} , and SW_{in} in W m^{-2} ; obtained from a ventilated 4-way CNR1 radiometer, Kipp & Zonen B.V., Delft, The Netherlands). Precipitation was measured every 30 min at 0.5 m a.g.l. (model 15188H, Lamprecht meteo GmbH, Göttingen, Germany). The horizontal visibility (in m) was measured at 2 m a.g.l. every 10 s with a fog sensor (MiniOFS, Optical Sensors Inc., Göteborg, Sweden) and a present weather detector (PWD10, Vaisala Oyj, Vantaa, Finland), and was then processed to 1 min averages.

Net radiation flux (R_n , W m^{-2} ; Eq. 1) is quantified as:

$$R_n = \text{LW}_{\text{in}} + \text{SW}_{\text{in}} - \text{LW}_{\text{out}} - \text{SW}_{\text{out}} \quad (1)$$

The energy balance of the grassland surface (Eq. 2) is expressed as:

$$R_n = H + \text{LE} + G + \Delta Q \quad (2)$$

where ΔQ is the budget closure term which accounts for all unmeasured advective fluxes and for the measurement errors of the measured fluxes. When fog occurs or dew drips to the optical windows of the IRGA, LE measurements become unrealistic and cannot be analyzed quantitatively.

The surface temperature (T_0 ; Eq. 3) is determined following Stefan-Boltzmann's law as (Moene and van Dam, 2014):

$$T_0 = \sqrt[4]{\frac{\text{LW}_{\text{out}} - (1 - \epsilon) \cdot \text{LW}_{\text{in}}}{\epsilon \cdot \sigma}} - 273.15, \quad (3)$$

where σ is Stefan-Boltzmann constant at $5.67 \cdot 10^{-8} \text{ W m}^{-2} \text{ K}^{-1}$. We are interested in the meteorological variability during fog periods, so we simply assume wet vegetation surfaces given an emissivity (ϵ) of 0.98 following López et al. (2012) for interpreting T_0 .

The saturation specific humidity (q_0 in g kg⁻¹; Eq. 4) at surface temperature (T_0 in °C) is given by (Garratt, 1992):

$$q_0 = \frac{622 \cdot p}{e_{s0}} - 0.378 \cdot e_{s0}, \quad (4)$$

where p in hPa is air pressure, and e_{s0} in hPa is saturation vapor pressure at T_0 given by Eq. 5 (Garratt, 1992):

$$e_{s0} = 6.112 \cdot \exp\left(\frac{17.67 \cdot T_0}{T_0 + 243.5}\right) \quad (5)$$

Fog was thought to occur when visibility was shorter than 1000 m; photos were taken by two thermal webcams (INSTAR Deutschland GmbH, Hünstetten, Germany), and the images were used to remove artifacts in visibility measurements related to disturbance by anthropogenic and animal activities; temperature ($T_{2\text{m}} > T_0$ at the beginning of fog stages during nighttime) and humidity ($\text{RH}_{2\text{m}} = 100\%$) measurements was used to double check the occurrence of fog. Dew was detected to occur when $T_{2\text{m}} > T_0$, and combined dew and fog with the additional conditions of visibility < 1000 m (excluding anthropogenic and animal

disturbances by thermal cameras).

2.2. Isotope measurements

The isotopic composition ($\delta^{18}\text{O}_v$ and $\delta^2\text{H}_v$) and the volumetric mixing ratio (r_v in mmol mol^{-1}) of the atmospheric water vapor were measured at 0.5–1 Hz using a cavity ring-down laser absorption spectrometer (L2130-i, Picarro Inc., Santa Clara, CA, USA). Ambient air was pulled into the L2130-i through a PTFE-filter inlet (FS-15-100 and TF50, Solberg International Ltd., Itasca, IL, USA) fixed at 6 m a.g.l., and a PTFE intake hose (1/4 inch of outer diameter; thermally isolated and heated using a resistive heating wire to prevent condensation and minimize the response time of the inlet system). An external membrane pump with a flow rate of 9 L min^{-1} (N022, KNF Neuberger GmbH, Freiburg, Germany) was used to maintain turbulent flow in the tube to minimize memory effects of the inlet system. Measurements of $\delta^{18}\text{O}_v$, $\delta^2\text{H}_v$ and r_v were made using a flow split with a flow rate of 300 mL min^{-1} through the L2130-i cavity. The response time of the L2130-i in this setup was on the order of 10 s according to Aemisegger et al. (2012). To correct for instrument drifts and to normalize the data to the international VSMOW-SLAP (Standard Light Antarctic Precipitation) scale, the raw data were calibrated using a Standard Delivery Module (SDM; A0101, Picarro Inc., Santa Clara, CA, USA) by performing two-point calibrations using two liquid standards (Aemisegger et al., 2012). The overall random uncertainties of $\delta^{18}\text{O}_v$ and $\delta^2\text{H}_v$ measurements were 0.2‰ and 0.8‰, respectively. For more details about the uncertainty quantification, see Aemisegger et al. (2012). According to our previous study (Li et al., 2021), the isotope composition of fog droplets taken from vegetation surfaces measured by an isotope ratio mass spectrometer (IRMS, DELTAplusXP, Finnigan MAT, Bremen, Germany) were in equilibrium with water vapor isotopes measured by L2130-i, indicating the reliability of our water vapor isotope measurement used for investigating fog evolution.

Calibrated $\delta^{18}\text{O}_v$ and $\delta^2\text{H}_v$ were then averaged over 10 min intervals, and the corresponding d_v (Eq. 6) is calculated as (Clark and Fritz, 1997; Dansgaard, 1964):

$$d = \delta^2\text{H} - 8 \cdot \delta^{18}\text{O} \quad (6)$$

The transport potentials of water are taken as normalized relative humidity values. This relative humidity is defined as the ratio of specific humidity at any altitude, to that of saturated air at the pressure and temperature of the interface (Craig and Gordon, 1965). Following this concept, atmospheric specific humidity (q_a in g kg^{-1}) was derived from r_v , hence the surface relative humidity (RH_0 in %; Eq. 7) is given by:

$$\text{RH}_0 = \frac{q_a}{q_0} = \frac{r_v \cdot M_v \cdot a}{r_v \cdot M_v \cdot a + M_d} \quad (7)$$

where $M_v = 0.018015 \text{ kg mol}^{-1}$ is the mole weight of water vapor, $M_d = 0.028965 \text{ kg mol}^{-1}$ is the mole weight for dry air, and 'a' is a unit conversion factor ($10^{-3} \text{ mol mmol}^{-1} \cdot 103 \text{ g kg}^{-1}$). We note that with dew and fog formations, the transport potential of water vapor is directed from atmosphere to the surface, hence RH_0 can be $> 100\%$ under these conditions.

2.3. Temperature profile and cloud interpretation

To get an estimate for the evolution of the atmospheric boundary layer above the CH-CHA site, we extracted vertical profiles of temperature and liquid water content (LWC) from COSMO-1 (Consortium for Small-scale Modeling) analyses. COSMO-1 is the operational numerical weather prediction model run by the Federal Office of Meteorology and Climatology in Switzerland (MeteoSwiss). COSMO-1 analyses describing the current state of the atmosphere are obtained from a continuous

observation assimilation cycle employing a nudging algorithm (Schraff and Hess, 2012). Temperature and humidity observations from both radio soundings and surface stations are assimilated. Fog, especially local-scale shallow fog, is challenging to be modeled accurately. COSMO-1 is known to have a systematic tendency to underestimate fog occurrence; this is however less severe for the analyses compared to forecasts (Westerhuis et al., 2020).

COSMO-1 analysis temperature profiles were used to illustrate shallow temperature inversions and their transition to well-mixed adiabatic layers in the near-surface atmosphere. For cases featuring substantial clouds, i.e. frontal clouds or extensive low stratus, the presence of clouds was interpreted from the maximum LWC ($\text{LWC}_{\text{max}} > 0$ in a LWC profile. Vertical profiles of the LWC were used to depict the transition from fog which lifts into elevated low stratus.

When interpreting model data, its resolution has to be kept in mind: COSMO-1 features a horizontal resolution of 1.1 km and has 80 vertical levels with a spacing of 20–170 m in the lowest 3 km. The difference between the elevation of the grid cell (408.5 m a.s.l.) closest to CH-CHA (393 m a.s.l.) and the measurement site itself is 15.5 m due to deviations in the representation of topography in the COSMO-1 model from the real topography. The modelled temperature and LWC profiles start at 10 m above the surface, thus resulting in a height difference of ~ 20 m between the isotopic measurements (6 m a.g.l. at CH-CHA) and modelled variables.

In addition to the COSMO-1 analyses, the locally measured surface energy fluxes at CH-CHA (LW_{in} and H) were analyzed to identify the presence of fog or clouds. Furthermore, together with the visibility measurements, they were used to check the validity of the selected model profiles. Additionally, cloud base height (Fig. A1; data was provided by REGA – Swiss Air-Rescue) retrieved from a ceilometer (CL31, Vaisala, Bonn, Germany) located at Nottwil, (22 km in the southwest of the CH-CHA site) was consulted to corroborate the regional-scale cloud evolution.

2.4. Fog and cloud events

In 2018, we selected four radiation fog events on 28–29 July (event 1), 10–11 October (event 2), 26–27 September (event 3), and 19–20 October (event 4), as well as one cloudy event on 23–24 September (event 5). Precipitation was absent during the 24-h observation periods of each event (i.e., from 12:00 to 12:00 CET the next day). Times are reported in CET (UTC + 01:00). All fog events (events 1–4) in this study occurred in conditions with saturated air at 2 m a.g.l. ($\text{RH}_{2\text{m}} = 100\%$). According to the atmospheric ($\text{RH}_{2\text{m}}$) and humidity conditions (RH_0), we classified the five events as:

- (1) Event 1 was shallow radiation fog occurring shortly before sunrise with $\text{RH}_{2\text{m}} = 100\%$ and $\text{RH}_0 \geq 100\%$, and fog dissipated shortly after sunrise when $\text{RH}_0 < 100\%$.
- (2) Event 2 and event 3 started from shallow radiation fog during nighttime with $\text{RH}_{2\text{m}} = 100\%$ and $\text{RH}_0 \geq 100\%$; transition of fog was characterized by $\text{RH}_{2\text{m}} = 100\%$ and decreasing RH_0 from levels $> 100\%$ to $< 100\%$; deep fog developed when $\text{RH}_{2\text{m}} = 100\%$ and $\text{RH}_0 < 100\%$.
- (3) Event 4 started from shallow radiation fog during nighttime which gradually became denser with $\text{RH}_{2\text{m}} = 100\%$ and $\text{RH}_0 \geq 100\%$; fog lifted to stratus cloud around midnight with $\text{RH}_{2\text{m}} = 100\%$ and $\text{RH}_0 < 100\%$.
- (4) Event 5 had no fog with cloud frontal clouds in conditions of $\text{RH}_{2\text{m}} = 100\%$ and $\text{RH}_0 < 100\%$.

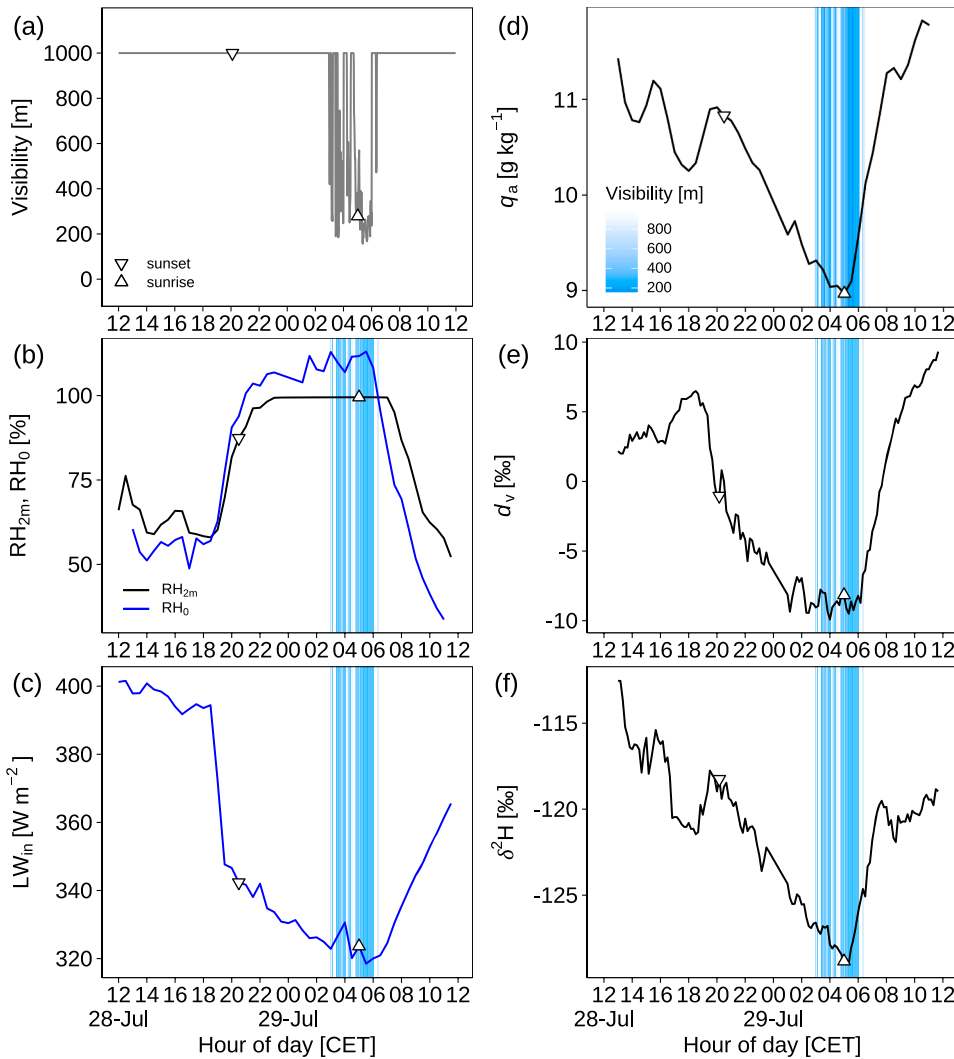


Fig. 3. Isotopic and meteorological variables during event 1 (28–29 July 2018) with shallow radiation fog occurring and dissipating around sunrise: (a) Fog occurrence with horizontal visibility < 1000 m (1-min averages) measured at ground level; visibility higher than 1000 m was shown as 1000 m. (b) 30-min relative humidity (RH_{2m}) measured at 2 m a.g.l., and simulated surface relative humidity (RH₀) at surface temperature (T₀). (c) 30-min incoming longwave radiation flux (LW_{in}) measured at 2 m a.g.l.. (d) 30-min specific humidity (q_a) derived from volumetric water vapor mixing ratio measured at 6 m a.g.l.. (e–f) 10-min isotopic composition (secondary variable d_v = δ²H_v – 8δ¹⁸O_v, and measured δ²H_v) of atmospheric water vapor at 6 m a.g.l..

2.5. Air parcel cooling and mixing models

The δ²H_v–q_a relations can be simulated by Eq. 8 using a Rayleigh condensation model (Noone, 2012):

$$\delta^2 H_v \approx \delta^2 H_{v,0} + \left[\frac{\alpha \epsilon}{1 - \alpha(1 - \epsilon)} - 1 \right] \times \ln \left[\frac{\alpha l_0 + q_a - \alpha(1 - \epsilon)(q_a - q_{a,0})}{\alpha l_0 + q_{a,0}} \right], \quad (8)$$

where deposition efficiency (ε) is the deposition rate of condensate proportional to condensation rate; l is the mass of condensate; subscript ‘0’ represents initial state values at the beginning of condensation; α is the effective fraction calculated from equilibrium fractionation factor α_e (Majoube, 1971) at dew-point temperature given by Eq. 9:

$$\alpha = (1 + \phi)\alpha_e, \quad (9)$$

where φ is the degree to which α deviates from equilibrium; considering the case when some fraction of the precipitation (f) evaporates, φ is given by Eq. 10:

$$\phi = \frac{f}{1 - f} \left[1 - \frac{\alpha_k}{\alpha_c} \frac{1 - h_r \left(\frac{R_b}{R} \right)}{1 - h_r} \right] \quad (10)$$

The h_r is the relative humidity near the dew or fog droplets; α_k is the

kinetic fractionation (Dongmann et al., 1974); R_b is the isotope ratio of the vapor through which the droplets deposit; R is the isotope ratio of condensed vapor; here both R_b and R are assumed as the isotope ratio of atmospheric water vapor in the near-surface air parcel.

The mass of condensate l (Eq. 11) can be calculated as:

$$l_0 = l_0 + (1 - \epsilon)(q_{a,0} - q_a) \quad (11)$$

With fog formation, ε is lower than unity (here given ε = 0.1 as extreme condition), hence the condensation process for fog formation is regarded as a closed-system Rayleigh condensation model.

With dew formation, ε is unity (ε = 1), and the condensation process for dew formation is regarded as an open-system Rayleigh condensation model (Eq. 12) approximate as:

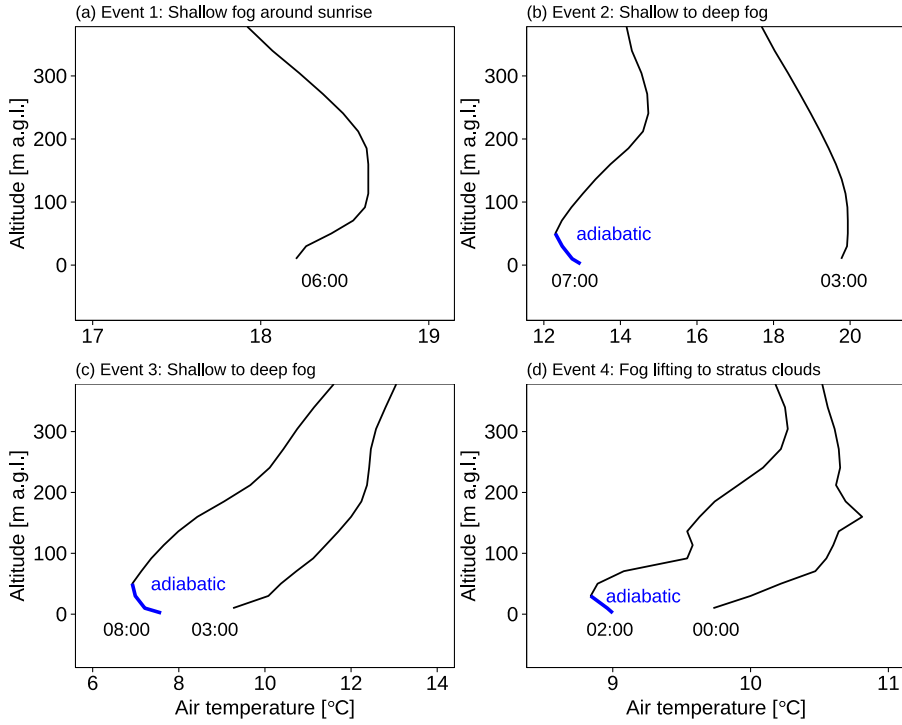


Fig. 4. Vertical profiles of air temperature during the four fog events using COSMO-1 analyses. (a) Event 1 on 29–30 July 2018: Shallow radiation fog occurring and dissipating around sunrise. (b) Event 2 on 10–11 October 2018: Shallow radiation fog transitioned into deep radiation fog which persisted after sunrise. (c) Event 3 on 26–27 September 2018: Shallow radiation fog transitioned to deep radiation fog which persisted after sunrise. (d) Event 4 on 19–20 October 2018: Fog lifted to stratus clouds. With the occurrence of deep radiation fog in events 2 and 3, a moist adiabatic temperature profile developed as marked in blue; adiabatic temperature profile in event 4 developed during the elevated stratus period.

Table 1

Summary of specific humidity (q_a) and isotopic (δ^2H_v and d_v) changes during four fog events 1–4 and one cloudy event 5. The mean \pm standard deviation indicates constant or fluctuated variables in $\%$ and $g\ kg^{-1}$, whilst the formats in the unit of $\% h^{-1}$ and $g\ kg^{-1}\ h^{-1}$ indicate the increasing or decreasing trends of variables. The magnitudes of temporal variability in δ^2H_v and d_v are the difference between the respective maximum and minimum during the fog periods for events 1–4 and during the cloudy period for event 5. RH_0 , normalized surface relative humidity quantifying the transport potential of water at land-atmosphere interface. Dense fog period in event 4 might be deep fog but below the vertical ranges of COSMO-1 analyses that we used for interpreting moist adiabatic temperature profile as the indicator for deep fog.

Event	Date	Sunrise [CET]	Fog stage	Period [CET]	Changes of q_a	Changes of d_v	Changes of δ^2H_v	Change magnitude	Dissipation
Event 1	28–29 Jul	05:01	shallow	03:00 to sunrise Sunrise to 06:00	$-0.17\ g\ kg^{-1}\ h^{-1}$ $0.61\ g\ kg^{-1}\ h^{-1}$	$-8.7 \pm 0.3\%$ $-8.5 \pm 0.6\%$	$-0.9\% h^{-1}$ $3.5\% h^{-1}$	3.5‰ for δ^2H_v ; 1.4‰ for d_v	$RH_0 < 100\%$
Event 2	10–11 Oct	06:39	shallow transition deep	03:00 to 04:30 04:30 to 05:30 05:30 to 10:00	$-0.16\ g\ kg^{-1}\ h^{-1}$ $0.74\ g\ kg^{-1}\ h^{-1}$ $0.38\ g\ kg^{-1}\ h^{-1}$	$-0.4\% h^{-1}$ $4.1\% h^{-1}$ $6.8 \pm 0.5\%$	$-1.1\% h^{-1}$ $1.6\% h^{-1}$ $1.9\% h^{-1}$	10.1‰ for δ^2H_v ; 5.2‰ for d_v	$RH_0 < 100\%$
Event 3	26–27 Sep	06:20	shallow transition deep deep	22:00 to 02:00 02:00 to 03:30 03:30 to sunrise Sunrise to 10:00	$-0.27\ g\ kg^{-1}\ h^{-1}$ $5.94 \pm 0.11\ g\ kg^{-1}\ h^{-1}$ $-0.12\ g\ kg^{-1}\ h^{-1}$ $0.57\ g\ kg^{-1}\ h^{-1}$	$-2.7 \pm 0.5\%$ $4.0\% h^{-1}$ $3.6 \pm 0.5\%$ $1.2\% h^{-1}$	$-2.2\% h^{-1}$ $-1.2\% h^{-1}$ $-2.3\% h^{-1}$ $6.5\% h^{-1}$	24.6‰ for δ^2H_v ; 11.3‰ for d_v	$RH_0 < 100\%$
Event 4	19–20 Oct	06:52	shallow dense	18:30 to 20:00 20:00 to 00:00	$-0.46\ g\ kg^{-1}\ h^{-1}$ $6.02 \pm 0.23\ g\ kg^{-1}\ h^{-1}$	$3.1 \pm 0.8\%$ $0.6\% h^{-1}$	$-2.0\% h^{-1}$ $-0.9\% h^{-1}$	9.4‰ for δ^2H_v ; 4.0‰ for d_v	Lifting to stratus clouds
Event 5	23–24 Sep	06:16	no fog	20:00 to 00:00 00:00 to 06:00 06:00 to 10:00	$-0.37\ g\ kg^{-1}\ h^{-1}$ $-0.37\ g\ kg^{-1}\ h^{-1}$ $-0.37\ g\ kg^{-1}\ h^{-1}$	$-2.2\% h^{-1}$ $8.3 \pm 1.2\%$ $1.7\% h^{-1}$	$-3.4\% h^{-1}$ $-147.9 \pm 3.2\%$ $-5.7\% h^{-1}$	34.6‰ for δ^2H_v ; 9.3‰ for d_v	No fog with cold frontal clouds

$$\delta^2H_v \approx \delta^2H_{v,0} + (\alpha - 1) \ln\left(\frac{q_a}{q_{a,0}}\right). \quad (12)$$

During the fog transition stage, δ^2H_v was simulated from q_a by an air mass mixing model with the entrainment of air from aloft into the fog

layer, and is given by Eq. 13:

$$\delta^2H_v = q_{a,0} (\delta^2H_{v,0} - \delta^2H_{v,F}) \frac{1}{q_a} + \delta^2H_{v,F}, \quad (13)$$

where subscript ‘F’ denotes the flux into the near-surface air parcel,

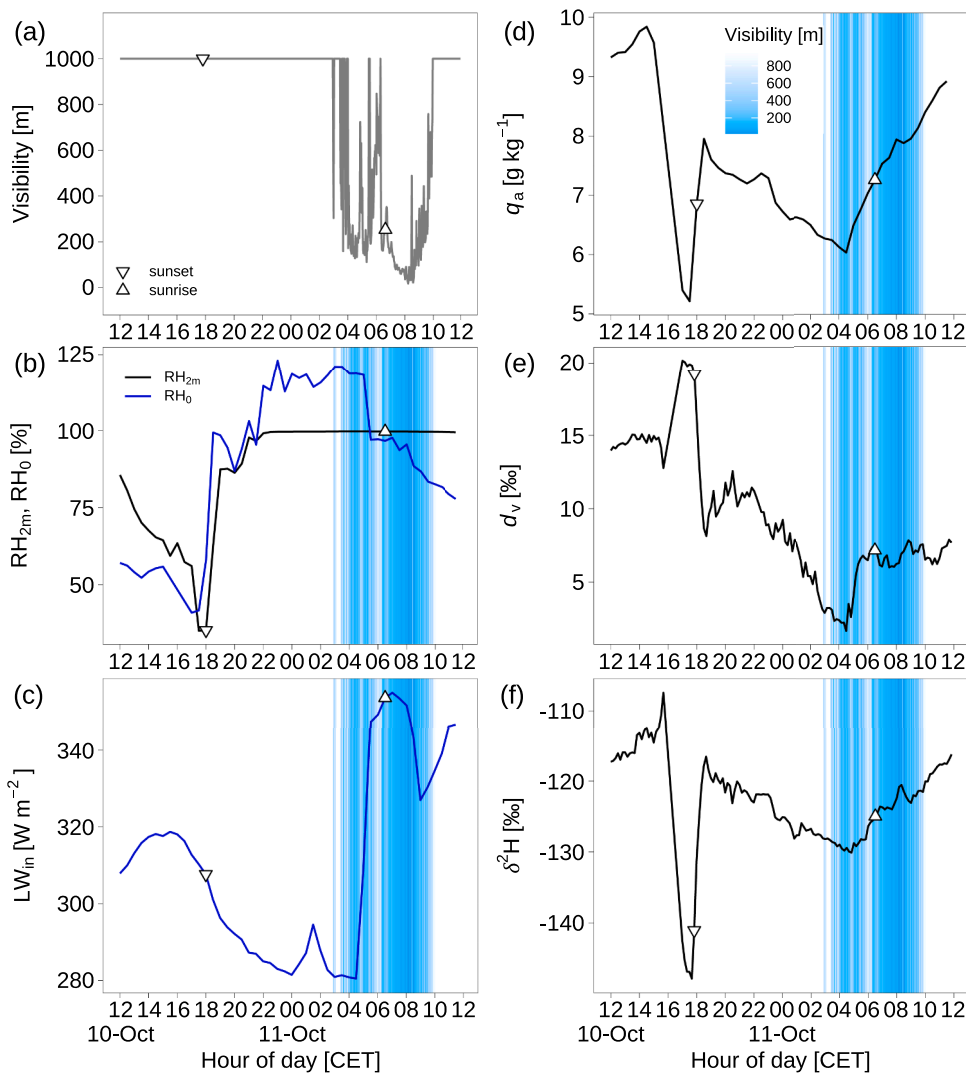


Fig. 5. Isotopic and meteorological variability during event 2 (10–11 October 2018) with shallow radiation fog transitioning to deep radiation fog which persisted after sunrise. (a) Fog occurrence with horizontal visibility < 1000 m (1-min averages) measured at ground level; visibility higher than 1000 m was shown as 1000 m. (b) 30-min relative humidity (RH_{2m}) measured at 2 m a.g.l., and simulated surface relative humidity (RH_0) at surface temperature (T_0). (c) 30-min incoming longwave radiation flux (LW_{in}) measured at 2 m a.g.l.. (d) 30-min specific humidity (q_a) derived from volumetric water vapor mixing ratio measured at 6 m a.g.l.. (e–f) 10-min isotopic composition (secondary variable $d_v = \delta^2H_v - 8\delta^{18}O_v$, and measured δ^2H_v) of atmospheric water vapor at 6 m a.g.l..

hence $\delta^2H_v \cdot F$ equals the values of δ^2H_v at the beginning of condensation (i.e., dew formation).

3. Results

In the following sections the isotope signals and moist processes affecting the different stages of radiation fog evolution, i.e., shallow radiation fog (event 1, Section 3.1), transition to deep fog with dominating entrainment (event 2, Section 3.2), transition to deep fog with dominating effect of condensation (event 3, Section 3.3), fog lifting (event 4, Section 3.4), and no fog with frontal clouds (event 5, Section 3.5) are interpreted.

3.1. Shallow radiation fog around sunrise

On a clear and calm night ($u_{2m} < 0.6 \text{ m s}^{-1}$; Fig. A2) during Event 1 (28–29 July), shallow radiation fog (visibility < 1000 m; Fig. 3a) intermittently occurred with dew formation from 03:00 to 06:00 with a temperature inversion within 110 m above the surface (Fig. 4a). The fog occurred in conditions of $RH_{2m} = 100\%$ and $RH_0 = 112\% \pm 2\%$ (Fig. 3b), and LW_{in} fluctuated around 324 W m^{-2} (Fig. 3c). Fog occurrence induced decreasing q_a and δ^2H_v combined with constant d_v ($-8.7 \pm 0.3\%$) at low levels of the 24-h period due to ongoing condensation (Fig. 3; Table 1).

The low values of d_v (Fig. 3e) during the fog period were reached due

to continuous dew formation before the appearance of the fog (Fig. 2a). With slightly decreasing LW_{in} from around sunset to 03:00, linearly decreasing q_a and δ^2H_v went along with dew formation in conditions of $RH_{2m} \leq 100\%$ and $RH_0 > 100\%$ (Fig. 3). The variability of d_v during this pre-fog period is strongly tied to the variability in RH_0 values. With RH_0 increasing above 100%, d_v exponentially decreased and δ^2H_v decreased linearly (Fig. 3) due to condensation on the surface with the air being super-saturated with respect to the surface temperature. When the shallow radiation fog appeared, d_v remained constant with constant $RH_0 > 100\%$ and $RH_{2m} = 100\%$ (Fig. 3), suggesting that continued condensation (dew formation) in equilibrium conditions promoted fog formation.

The shallow fog dissipated at 06:00 in conditions of $RH_{2m} = 100\%$ and $RH_0 < 100\%$ (Fig. 3b), due to the evaporation of dew and fog droplets occurring after sunrise due to SW warming (Fig. 2a). During a short period before fog dissipation, i.e., from sunrise to 06:00 (Fig. 3), q_a and δ^2H_v rapidly increased by the respective rate of 0.61 g kg h^{-1} and $3.5\% \text{ h}^{-1}$, while d_v stayed low (-8.5%), indicating that fog droplets previously formed from low d_v started to evaporate (Fig. 2a) and thus imprinting their high δ^2H (and low d_v) on the near-surface atmospheric vapor. Later on, after the fog dissipated completely, d_v increased (Fig. 3e) as well, which can be explained by the onset of evapotranspiration (Fig. 2a) as indicated in the steep increase in q_a (Fig. 3d).

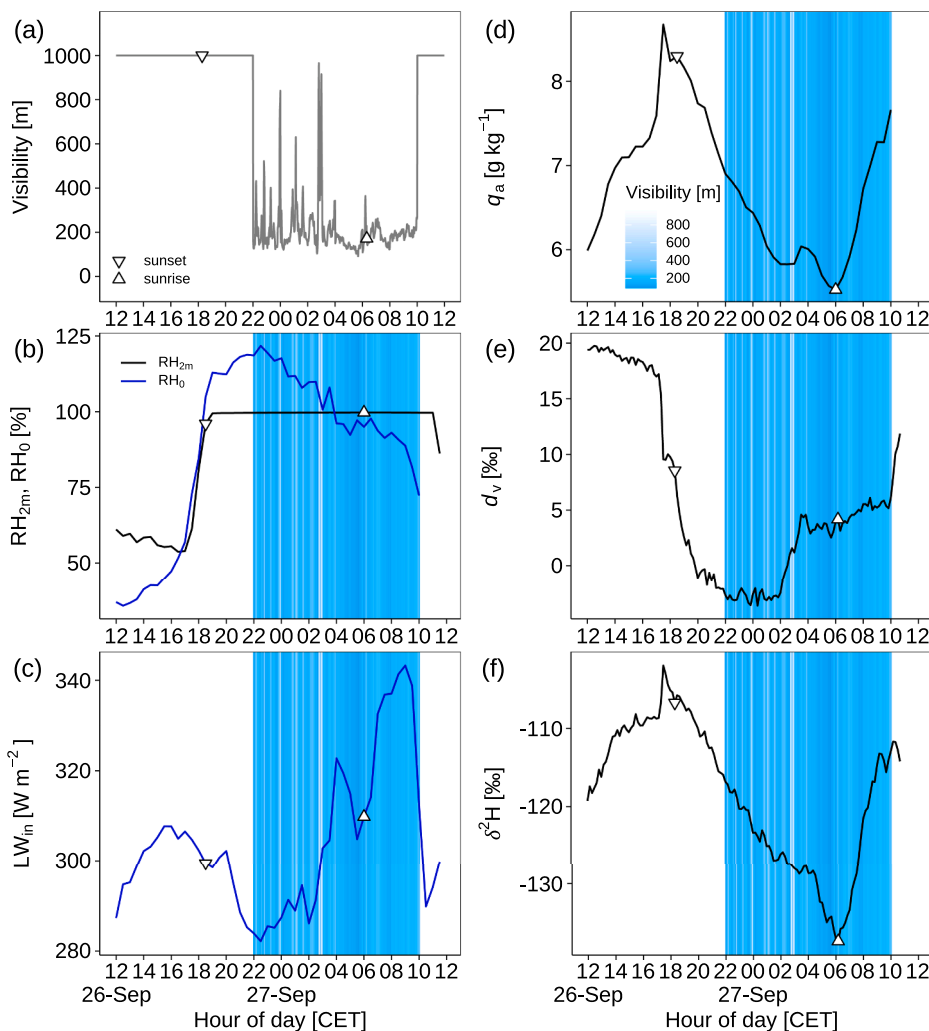


Fig. 6. Isotopic and meteorological variability during event 3 (26–27 September 2018) with shallow radiation fog transitioning to deep radiation fog, which persisted after sunrise: (a) Fog occurrence with horizontal visibility < 1000 m (1-min averages) measured at ground level; visibility higher than 1000 m was shown as 1000 m. (b) 30-min relative humidity (RH_{2m}) measured at 2 m a.g.l., and simulated surface relative humidity (RH_0) at surface temperature (T_0). (c) 30-min incoming longwave radiation flux (LW_{in}) measured at 2 m a.g.l. (d) 30-min specific humidity (q_a) derived from volumetric water vapor mixing ratio measured at 6 m a.g.l. (e–f) 10-min isotopic composition (secondary variable $d_v = \delta^2H_v - 8\delta^{18}O_v$, and measured δ^2H_v) of atmospheric water vapor at 6 m a.g.l..

3.2. Radiation fog transitioning from shallow to deep fog, and fog-top entrainment dominating over condensation during fog transition

While the fog during event 1 lasted only for 3 h (Fig. 3), event 2 (10–11 October) is characterized by a longer lasting radiation fog. Fog in event 2 formed at 03:00, lasted for 7 h, and dissipated 4 h after sunrise at 10:00 (Fig. 5). This fog period was associated with clear-sky conditions above. The life cycle of the radiation fog in event 2 features three stages, i.e., shallow fog (from 03:00 to 04:30; Fig. 5) with a temperature inversion in the near-surface atmosphere (Fig. 4b), fog transition (from 04:30 to 05:30; Fig. 5), and deep fog (from 05:30 to 10:00; Fig. 5) with a moist adiabatic temperature profile in the lowermost layer (50 m) of the atmospheric boundary layer (Fig. 4b).

Shallow fog occurred intermittently (Fig. 5) with dew formation from 03:00 to 04:30 with $RH_{2m} = 100\%$ and constant RH_0 at values >100%. During this stage, q_a and δ^2H_v decreased, combined with slightly decreasing d_v (Fig. 5; Table 1).

The transition stage occurred from 04:30 to 05:30 with $RH_{2m} = 100\%$ (Fig. 5b). RH_0 strongly decreased from >100% down to 97% (Fig. 5b). During the fog transition, the steeply increasing LW_{in} from 281 to 354 $W m^{-2}$ (Fig. 5c) indicates the gradual thickening of the fog layer. In the shallow fog stage condensation caused decreasing q_a and δ^2H_v (Fig. 5d, f), while in the transition period, q_a , d_v , and δ^2H_v strongly increased (Fig. 5; Table 1). This can be explained by the entrainment of air at fog-top that dominated over condensation. Details will be discussed in Section 4.1.

After 2.5 h of fog onset, the environmental conditions were characterized by $RH_{2m} = 100\%$ and $RH_0 < 100\%$ (Fig. 5b). While the fog during event 1 dissipated under exactly these environmental conditions, in this case, fog developed from 05:30 and persisted until 10:00 in event 2 (Fig. 5b). During this deep fog stage, q_a linearly increased combined with constant d_v and slightly increasing δ^2H_v (Fig. 5; Table 1), which can be explained by the evaporation of fog droplets due to SW warming after sunrise in the fog-top region and entrainment of this negatively buoyant air induced by evaporative cooling (Fig. 2b). Decreasing LW_{in} and improving visibility (Fig. 5a, c) indicated fog erosion, which we can attribute to the deposition of fog droplets to the surface and the evaporation of fog droplets (Fig. 2b).

After fog dissipation at 10:00, the variability in d_v and δ^2H_v (Fig. 5b, c) remained similar as during the deep fog stage. SW_{in} (Fig. A3a) showed similar levels as during the foggy period, which might be due to the slow evaporation of dew and deposited fog droplets (Fig. 2b) from the surface as also indicated by the very low level of LE (Fig. A3f).

3.3. Radiation fog transitioning from shallow to deep fog, and condensation dominated over fog-top entrainment during fog transition

Compared to event 2 (Fig. 5), radiation fog started earlier at 22:00 (Fig. 6) during event 3 (26–27 September), and fog persisted until 4 h after sunrise (10:00; Fig. 6a). The earlier starting of fog in event 3 might be attributed to the weaker turbulence as indicated in u_{2m} ($0.2 \pm 0.1 m s^{-1}$) and u^* ($0.05 \pm 0.02 m s^{-1}$) as compared to that in event 2 ($u_{2m}: 0.3$

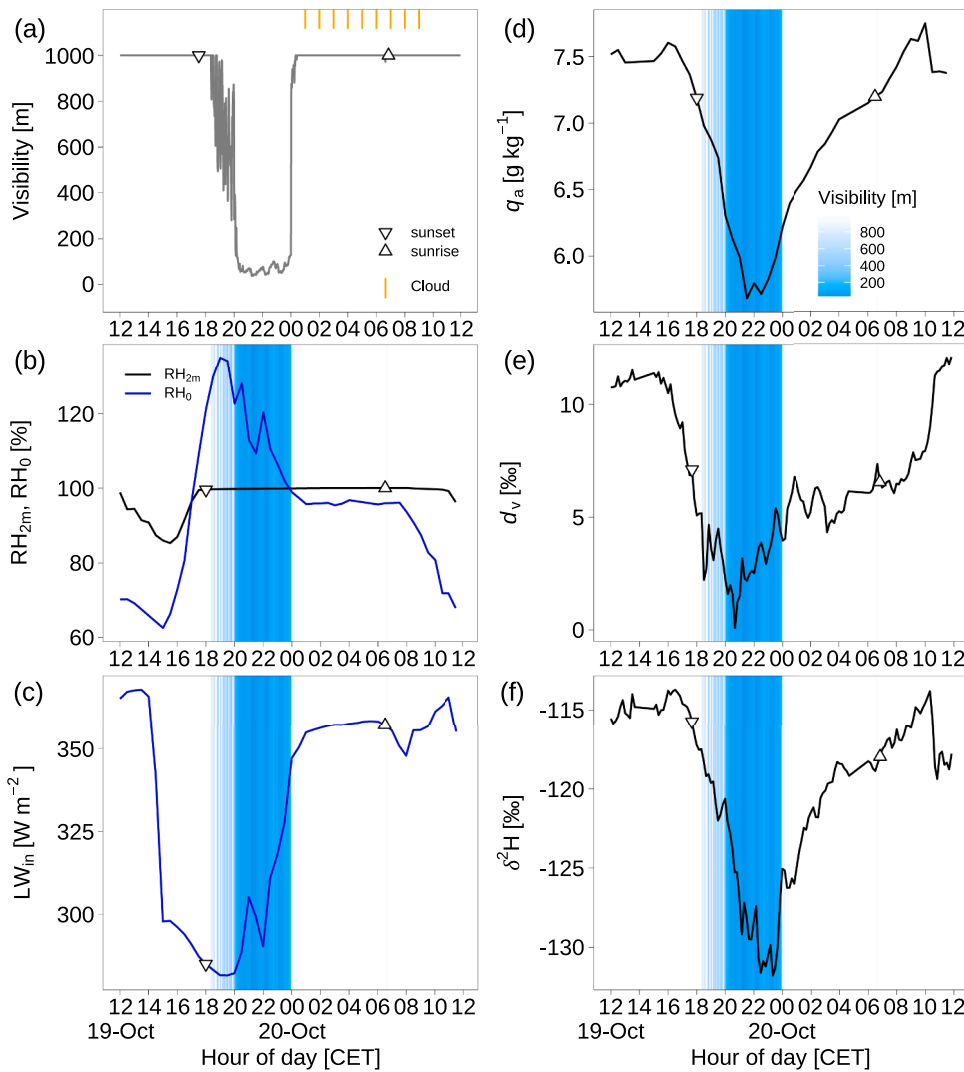


Fig. 7. Isotopic and meteorological variability during event 4 (19–20 October 2018) with fog transforming to elevated stratus; cloud was interpreted using COSMO-1 analyses when the maximum values of liquid water content (LWC_{max}) in a vertical profile was higher than zero: (a) Fog occurrence with horizontal visibility < 1000 m (1-min averages) measured at ground level; visibility higher than 1000 m was shown as 1000 m. (b) 30-min relative humidity (RH_{2m}) measured at 2 m a.g.l., and simulated surface relative humidity (RH_0) at surface temperature (T_0). (c) 30-min incoming long-wave radiation flux (LW_{in}) measured at 2 m a.g.l. (d) 30-min specific humidity (q_a) derived from volumetric water vapor mixing ratio measured at 6 m a.g.l. (e–f) 10-min isotopic composition (secondary variable $d_v = \delta^2H_v - 8\delta^{18}O_v$, and measured δ^2H_v) of atmospheric water vapor at 6 m a.g.l.

$\pm 0.1 \text{ m s}^{-1}$; u^* : $0.08 \pm 0.06 \text{ m s}^{-1}$; Fig. A2). The fog period in event 3 shows three stages (Fig. 6): (1) shallow fog (from 22:00 to 02:00) with a temperature inversion (Fig. 4c) in the near-surface atmosphere; (2) fog transition (from 02:00 to 03:30); and (3) deep fog (from 03:30 to 10:00) with a moist adiabatic temperature profile in the lowermost layer (50 m; Fig. 4c) of the atmospheric boundary layer.

During event 3, shallow fog occurred from 22:00 to 02:00 with $RH_{2m} = 100\%$ and constant $RH_0 > 100\%$ (Fig. 6b). Condensation during this fog stage induced steeply decreasing q_a and δ^2H_v , combined with constant d_v at low values of the 24-h period (Fig. 6; Table 1). In contrast to the shallow fog during event 1 (Fig. 3) and event 2 (Fig. 5) which intermittently occurred, shallow fog during event 3 was rather stable with visibility always < 1000 m (Fig. 6a). This can be explained by stronger condensation that enhanced fog persistence during event 3 and thus the fog layer was not disturbed by condensation-induced heat release. The stronger condensation is reflected in an enhanced decreasing rate of δ^2H_v (-2.2‰ h^{-1} for event 3, Fig. 6f; Table 1) compared to event 1 (-0.9‰ h^{-1} ; Fig. 3f; Table 1) and event 2 (-1.1‰ h^{-1} ; Fig. 5f; Table 1).

During fog transition from 02:00 to 03:30 in event 3 with $RH_{2m} = 100\%$ and steeply decreasing RH_0 at $> 100\%$, LW_{in} steeply increased (Fig. 6). The q_a varied around $5.94 \pm 0.11 \text{ g kg}^{-1}$ (Fig. 6; Table 1) combined with a steeply increasing d_v (4.0‰ h^{-1}) and slightly decreasing δ^2H_v (-1.2‰ h^{-1}). This was different from the fog transition during event 2 with increasing q_a , d_v and δ^2H_v (Fig. 6). The different humidity

and isotopic changes during the transition stages of event 2 and event 3 can be explained by a difference in the relative importance of condensation compared to entrainment of fog-top air (Fig. 2b), with the former dominating in event 3 (Fig. 6), while the latter dominated in event 2 (Fig. 5). Details will be discussed in Section 4.1.

The deep fog in event 3 developed after 5.5 h of fog onset (Fig. 6). This fog stage was further split into two sub-stages: (1) From 03:30 to sunrise, decreasing q_a and δ^2H_v combined with constant d_v (Fig. 6; Table 1), indicating continued condensation. (2) Whereas, from sunrise to 10:00, increasing q_a and δ^2H_v combined with slightly increasing d_v (Fig. 6; Table 1) can be induced by fog droplet evaporation combined with limited entrainment of evaporatively cooled air at fog-top (Fig. 2b). The stable visibility at 190 m and increasing LW_{in} (high up to 343 W m^{-2}) after sunrise (Fig. 6) indicated stronger condensation as compared to the deep fog period before sunrise.

With the dissipation of fog after 10:00 in event 3, d_v steeply increased (Fig. 6e), in contrast to the constant d_v after fog dissipation in event 2 (Fig. 5e). This can be attributed to the strength of turbulent mixing (Fig. A2b), surface fluxes (H and LE; Fig. A3e, f), and entrainment from the free troposphere. Details will be discussed in Section 4.1.

3.4. Fog lifted to stratus cloud on the night

Fog formed at 18:30 on 19 October (event 4; Fig. 7) and lifted to stratus clouds around midnight (Fig. 7a; Fig. 2c). The fog period in event

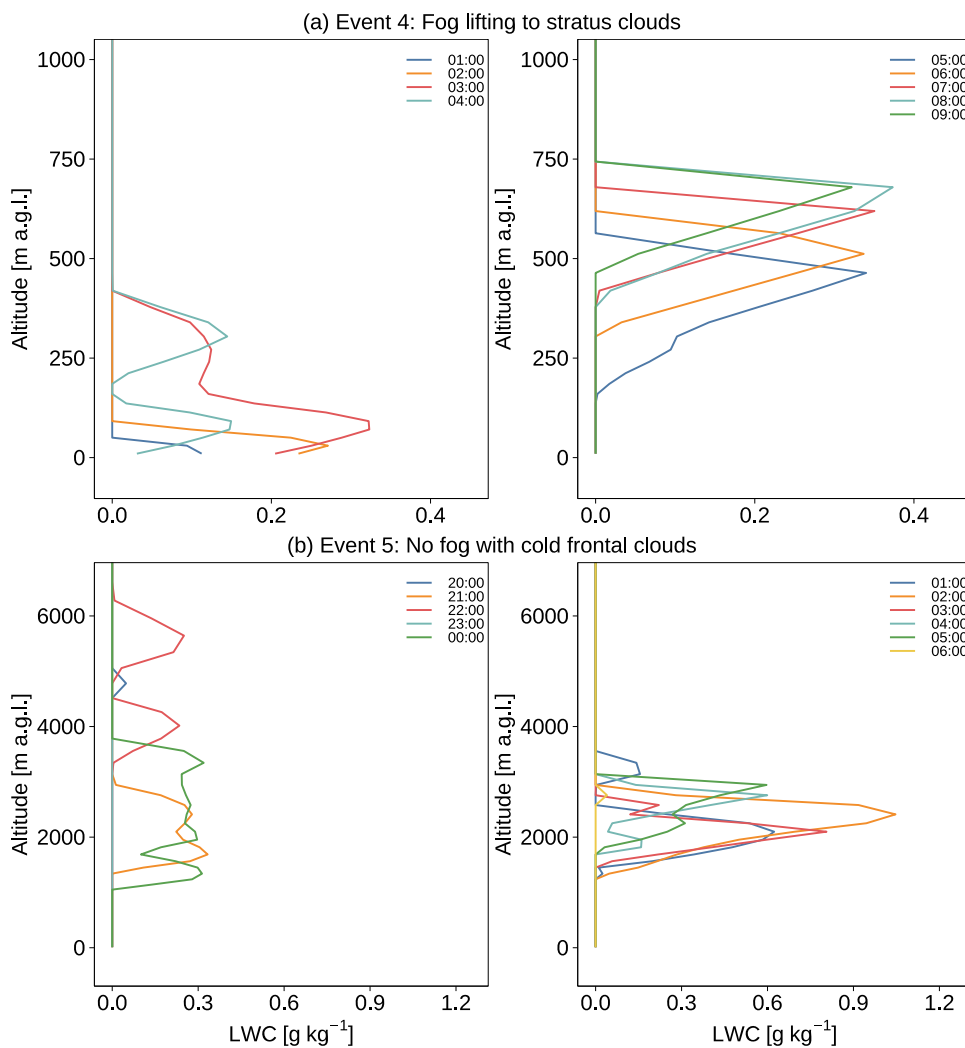


Fig. 8. Vertical profiles of liquid water content (LWC) extracted from COSMO-1 analyses during event 4 and event 5: (a) During event 4 (19–20 October 2018), modelled LWC evolution shows a time lag of 4 h. COSMO-1 shows fog from 01:00 to 04:00 (corresponding to observations from 21:00 to 00:00). The fog lifted to low stratus from 05:00 to 09:00 (corresponding to observations from 01:00 to 05:00) with LWC = 0 at the lowest model level. (b) During event 5 (23–24 September 2018), there was no fog with cold frontal clouds during 20:00 to 06:00. The numbers show the temperature ($^{\circ}\text{C}$) at the bottom of the cloud layers with color indicating the corresponding time.

4 included two stages: (1) intermittent shallow fog (from 18:30 to 20:00); and (2) transition towards dense fog (from 20:00 to 00:00) with a temperature inversion (Fig. 4d).

In conditions of $\text{RH}_{2\text{m}} = 100\%$ and $\text{RH}_0 > 100\%$ from 18:30 to 20:00, intermittent shallow fog induced decreasing q_a and $\delta^2\text{H}_v$ combined with constant d_v (Fig. 7; Table 1). From 20:00 till midnight with $\text{RH}_{2\text{m}} = 100\%$ and $\text{RH}_0 > 100\%$, fog became denser with almost constant visibility at around 80 m and a dramatic increasing LW_{in} from 282 to 347 W m^{-2} (Fig. 7). During this dense fog stage, RH_0 showed a decreasing trend combined with strong fluctuation, and q_a also varied considerably (Fig. 7). These conditions coincided with an increasing d_v with strong fluctuations, and a decreasing $\delta^2\text{H}_v$ with strong fluctuations (Fig. 7; Table 1). This humidity and isotopic variability combined with the dramatic increase in LW_{in} (Fig. 7c) indicates that shallow fog has transitioned into deep fog (from 22:00 to 00:00), but a moist adiabatic temperature profile can be seen in the COSMO-1 analysis at 02:00 (Fig. 4d). This suggested that the modelled LWC evolution shows a time lag of 4 h, but can nicely illustrate the transition from fog to low stratus clouds (Fig. 8a). COSMO-1 shows fog from 01:00 to 04:00 (corresponding to observations from 21:00 to 00:00) with LWC_{max} in the range of 0.11 to 0.32 g kg^{-1} (Fig. 8a). The fog lifted to low stratus from 05:00 to 09:00 (corresponding to observations from 01:00 to 05:00) with LWC = 0 at the lowest model level (Fig. 8a).

After fog lifting to stratus clouds, with $\text{RH}_{2\text{m}} = 100\%$ and $\text{RH}_0 < 100\%$ from 00:00 to 09:00 (Fig. 7), both q_a (0.16 $\text{g kg}^{-1} \text{h}^{-1}$) and $\delta^2\text{H}_v$ (1.1‰ h^{-1}) increased in combination with fluctuating d_v (6.0±0.8‰).

This can be explained by the evaporation of fog droplets in the fog layer and droplet deposition at the surface (Fig. 2c). LW_{in} increased to 355 W m^{-2} with fog lifting (Fig. 7c). The lifting of the fog to low stratus is associated with an increase of horizontal visibility to above 1000 m at ground level (Fig. 7a).

3.5. No fog with cold frontal clouds

Fog could not develop on the night of 23–24 September (event 5; Fig. 9) with cold frontal (Fig. A5e) clouds passing by at 1100–6300 m a. g.l. (Fig. 8b) and much stronger winds of up to 7.3 m s^{-1} (Fig. A2a) compared to the four fog events. Although $\text{RH}_{2\text{m}}$ remained constant at 100% (Fig. 9b) from midnight until around sunrise in event 5, RH_0 was $< 100\%$ (Fig. 9b) due to higher T_0 than $T_{2\text{m}}$ (Fig. A4e). These conditions suggested that water vapor in the near-surface atmosphere could not condense and consequently fog failed to develop. During the cloudy period from 20:00 to sunrise, q_a almost linearly decreased (Fig. 9d; Table 1), whilst the changes of d_v and $\delta^2\text{H}_v$ were related to atmospheric and surface humidity conditions in combination with the influence of the cold frontal clouds (Fig. A5e). From 20:00 to midnight, with LWC_{max} ranging from 0.05 to 0.33 g kg^{-1} at 1100–6300 m a.g.l. (Fig. 8b) and decreasing LW_{in} from 395 to 375 W m^{-2} (Fig. 9c), $\text{RH}_{2\text{m}}$ was $< 100\%$, and RH_0 steeply increased to values slightly below 100% (Fig. 9b) due to the faster cooling of the surface compared to the air during the cold frontal passage (Fig. A5e). These conditions induced steeply decreasing d_v and $\delta^2\text{H}_v$ (Fig. 9; Table 1). However, from 00:00 until 06:00 in event

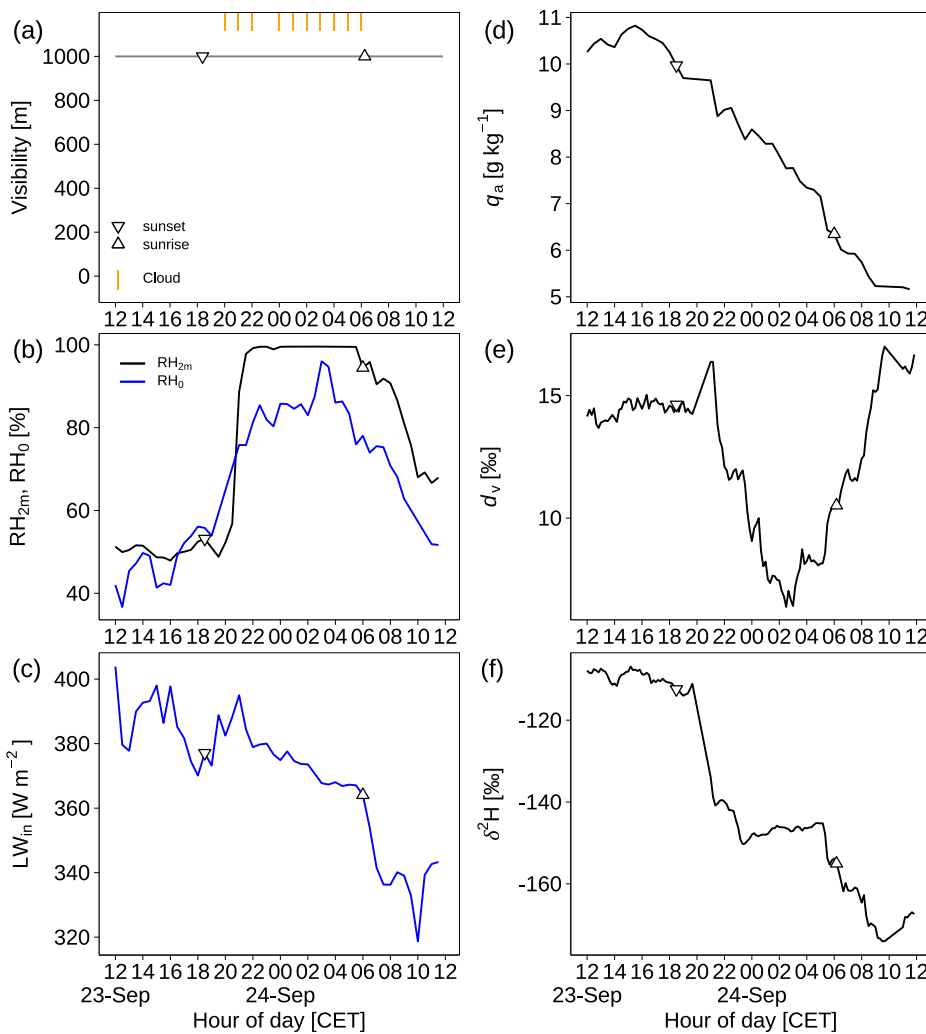


Fig. 9. Isotopic and meteorological variability during event 5 (23–24 September 2018) without fog but cloud frontal clouds; cloud was interpreted using COSMO-1 analyses when the maximum values of liquid water content (LWC_{max}) in a vertical profile was higher than zero: (a) No fog with horizontal visibility ≥ 1000 m (1-min average) measured at ground level; visibility higher than 1000 m was shown as 1000 m. (b) 30-min relative humidity (RH_{2m}) measured at 2 m a.g.l., and simulated surface relative humidity (RH_0) at surface temperature (T_0). (c) 30-min incoming longwave radiation flux (LW_{in}) measured at 2 m a.g.l.. (d) 30-min specific humidity (q_a) derived from volumetric water vapor mixing ratio measured at 6 m a.g.l.. (e–f) 10-min isotopic composition (secondary variable $d_v = \delta^2H_v - 8\delta^{18}O_v$, and measured δ^2H_v) of atmospheric water vapor at 6 m a.g.l.

5, with LWC_{max} increasing to $0.32\text{--}1.05\text{ g kg}^{-1}$ (Fig. 8b) at 1100–3600 a. g.l., RH_{2m} reached 100% and RH_0 varied around $87\pm 2\%$ (Fig. 9b). These environmental conditions during rain-free period induced fluctuating d_v around its 24-hour minimum value and δ^2H_v reached a plateau at $-147.9 \pm 3.2\text{‰}$ (Fig. 9; Table 1). After the disappearance of clouds from around sunrise to 10:00 (Fig. 9), LW_{in} dramatically decreased from 364 to 339 W m^{-2} , with decreasing RH_0 , increasing d_v (1.7‰ h^{-1}) in combination with decreasing δ^2H_v (-5.7‰ h^{-1}).

3.6. Comparing measured isotope signals with modelled signals using air parcel cooling and mixing models

Fig. 10 shows a comparison of $\delta^2H_v\text{--}q_a$ retrieved from measurements (dots) and simulations (lines) with a Rayleigh condensation model simulating condensation during fog formation with different deposition efficiencies. The measured and modeled $\delta^2H_v\text{--}q_a$ match well for events 1 and 3 with shallow radiation fog and transitioning to deep fog dominated by condensation, but differ for shallow fog transitioning to deep fog when entrainment dominating (events 2), or fog lifting to stratus cloud (event 4). This points out the challenge of modeling water vapor isotopes in transitioning fog layers when the influence of entrainment from fog-top plays an important role. In this case, advection in atmospheric layers that are decoupled from the surface plays an important role during fog transition into deeper fog layers.

The dominance of condensation or entrainment during fog transition was confirmed by comparing the measured δ^2H_v with simulated δ^2H_v

using a Rayleigh mixing model. During the transition fog stages, the predicted δ^2H_v using a Rayleigh mixing model matches well with measured δ^2H_v in event 2, indicating that mixing processes, i.e., the entrainment at fog-top was dominant over condensation during the fog transition in event 2 (Fig. 11a). As a comparison, the predicted δ^2H_v was higher than the measured δ^2H_v during the fog transition in event 3, which can be explained by condensation dominating over entrainment as indicated by the stronger decrease in measured δ^2H_v (Fig. 11b).

4. Discussion

4.1. Effect of humidity on fog evolution

Radiation fog in our study and in previous research (Kidron and Starinsky, 2019; Li et al., 2021; Smith et al., 2018) is found to occur in conditions of $RH_{2m} = 100\%$ (Fig. A6a), but once atmospheric humidity reached saturation, the fog evolution was closely linked to the variability of surface humidity conditions (RH_0 ; Fig. A6b). This stands in agreement with a recent study about dew deposition in oceanic environments (Thurnherr and Aemisegger, 2022). Conditions with $RH_{2m} = 100\%$ in event 1 caused the dissipation of shallow fog at around sunrise when $RH_0 < 100\%$ (Fig. 3b). As a comparison, in event 2 (Fig. 5b) and event 3 (Fig. 6b), when deep fog successfully developed in conditions of $RH_0 < 100\%$, the unsaturated surface conditions were associated with fog persistence after sunrise due to the negatively buoyant air sinking from fog-top (Fig. 2b), thereby supplying water vapor to the

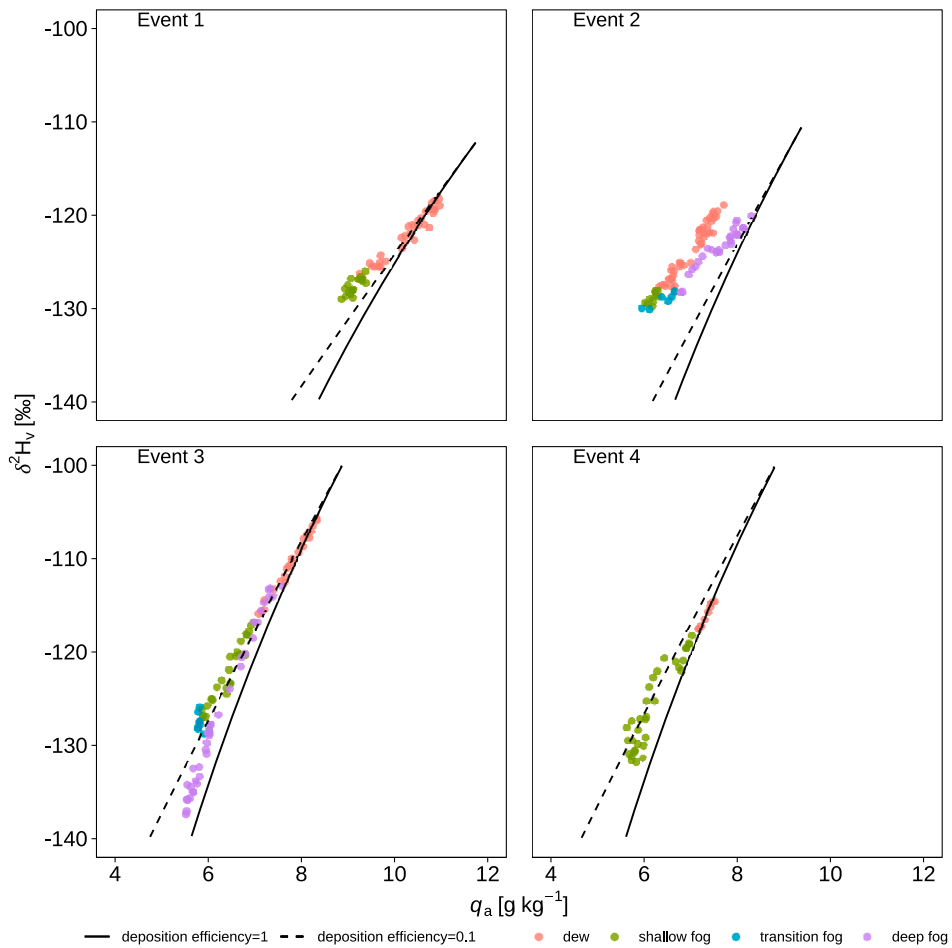


Fig. 10. Comparing the δ^2H_v - q_a relations predicted from a Rayleigh condensation model with measured data during the four fog events. Event 1 was a shallow radiation fog occurring and dissipating around sunrise; event 2 and event 3 were radiation fog events transiting from shallow to deep fog; event 4 started from a shallow radiation fog, and fog became denser and lifted to stratus cloud during nighttime.

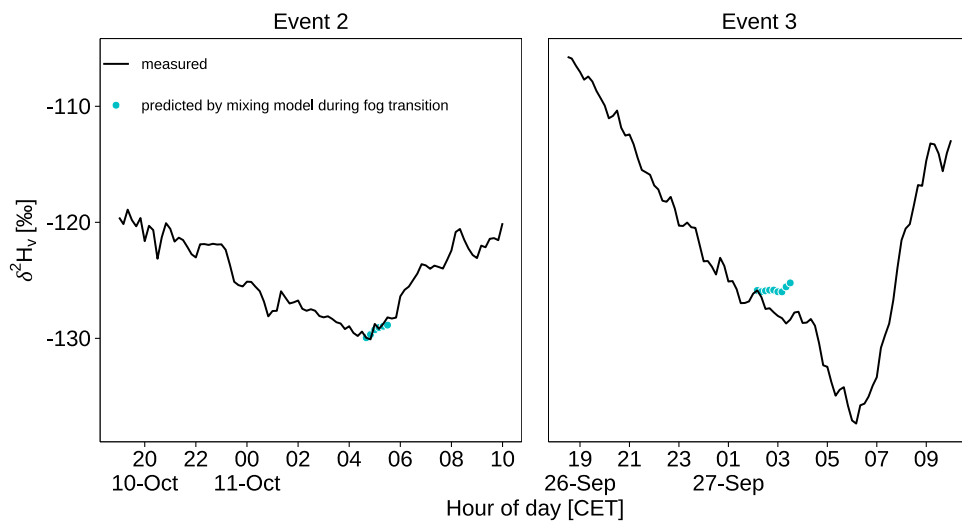


Fig. 11. Comparing the δ^2H_v during fog transition period in event 2 and event 3 with the simulated results by air parcel mixing model.

near-surface atmosphere. Fog lifting to stratus cloud resulted in increasing downwelling longwave radiation (LW_{in} ; Fig. 2b) in event 4, which caused the immediate dissipation of fog at ground level when $RH_0 < 100\%$ (Fig. 9b). Contrastingly, cold frontal clouds (Fig. A5e)

prohibited the formation of fog in event 5 with $RH_{2m} = 100\%$ in combination with unsaturated surface conditions ($RH_0 < 100\%$; Fig. 9b), due to strong winds.

4.2. Effect of fog evolution on water vapor isotopic signal

Intermittent occurrence of shallow fog has previously been attributed to the latent heat release by condensation (Price et al., 2018), which may have played a role during the fog period of event 1 (Fig. 3), and the shallow fog stage in event 2 (03:00 to 04:30; Fig. 5). Intermittent shallow fog was often associated with dew formation (Li et al., 2021). This kind of intermittent shallow fog occurring at around sunrise at the CH-CHA site is frequently observed in summer and early autumn given its location on a valley bottom (see more examples of this fog type in Fig. A7). Both dew and fog processes induced a linear decrease in $\delta^2\text{H}_v$ (Fig. 3f; Fig. 5f) due to condensation.

The transitional fog stages following shallow fog and before it evolves to deep fog in event 2 (Fig. 5), event 3 (Fig. 6), and event 4 (Fig. 7) were due to the sinking of negatively buoyant air from the fog-top to the ground surface (Smith et al., 2018) that imported additional water vapor from the overlaying atmosphere to the fog layer. Therefore, condensation during the transition stage was combined with a mixing effect (Fig. 2b) driven by entrainment (that further increases the stability of the near-surface layer) due to cloud top cooling. Equilibrium condensation with $\text{RH}_{2\text{m}} = 100\%$ generally does not change d_v but can induce a decrease in $\delta^2\text{H}_v$. Contrastingly, the effect of mixing air (as compared to the near-surface atmosphere) from the fog-top into the near-surface layer can cause increases in $\delta^2\text{H}_v$ and d_v in the near-surface atmosphere. The negatively buoyant air originating from the fog-top region may be associated with a higher $\delta^2\text{H}_v$ and d_v compared to near-surface air due to fog droplet evaporation, which could even evaporate fog droplets close to the ground surface. Furthermore, advection of moist and warm air from remote (e.g. more southerly areas; Fig. A5b) might also have contributed to the increase of $\delta^2\text{H}_v$ during this transition stage in event 2. With the combination of condensation and mixing processes, a steeply increasing $\delta^2\text{H}_v$ (Fig. 5f) during the transition stage of event 2 suggests that the mixing effect dominated over the condensation process. As a comparison, during the transition stage in event 3, a slight decrease in $\delta^2\text{H}_v$ (Fig. 6f), and a steeply increasing d_v (Fig. 6e) indicate that the condensation process dominated over the mixing process. Simulated $\delta^2\text{H}_v$ by the air parcel mixing model matched well with the measured values during fog transition in event 2, but overestimated $\delta^2\text{H}_v$ during the corresponding period of event 3 (Fig. 11). This result from simple isotope modelling confirms the respective mixing-dominant and condensation-dominant transition fog stages for event 2 and event 3.

Entrainment brought unsaturated air from the fog-top to the near-surface fog layer which consequently induced evaporation of fog droplets (Gultepe et al., 2007; Waersted et al., 2017). The second sub-stage of deep fog period (from sunrise to 10:00; Fig. 6) in event 3 might be due to the combined effect of fog evolution and entrainment from the troposphere. Entrainment acts to increase d_v in the near-surface atmosphere (Huang and Wen, 2014; Parkes et al., 2017). Therefore, in the second sub-stage of deep fog in event 3, entrainment caused a slightly increasing d_v (Fig. 6e).

The effect of entrainment from the troposphere on atmospheric water vapor dynamics was reflected in the changes of d_v after fog dissipation in event 2 (Fig. 5e) and event 3 (Fig. 6e). With the dissipation of fog after 10:00 of event 3, d_v steeply increased (Fig. 6e) which was in contrast to the constant d_v after fog dissipation in event 2 (Fig. 5e). These different temporal evolutions in d_v with fog dissipation were probably due to the different strength of the coupling between the entrainment from the free troposphere and surface fluxes as indicated by the higher SW_{in} ($601 \pm 114 \text{ W m}^{-2}$; Fig. A3a) pointing towards stronger entrainment in event 3 compared to that in event 2 (SW_{in} : $161 \pm 7 \text{ W m}^{-2}$, Fig. A3a).

Fog transition in event 2 (from 04:30 to 05:30; Fig. 5e) and event 3 (from 02:00 to 03:30; Fig. 6e) showed linearly increasing d_v , but the transition stage in event 4 showed increasing d_v in combination with strong fluctuations (Fig. 7e). This strongly fluctuating d_v in event 4 may

be explained by condensation in the fog layer combined with evaporation at the bottom of the fog layer, and thus might be an indicator for fog lifting to stratus clouds in the following hours (after 01:00; Fig. 7). Fog lifting to stratus clouds in event 4 might be due to the warming of latent heat release at the surface that eroded the bottom of fog layer, whilst latent heat release could not erode the fog in event 2 and event 3.

4.3. Drivers of water vapor isotope variability

Given the local vapor sources for radiation fog in our study, $\delta^2\text{H}-\delta^{18}\text{O}$ pairs distributed on the right-hand side of the LMWL (representing the $\delta^2\text{H}-\delta^{18}\text{O}$ pairs of precipitation; Fig. A8) at CH-CHA site due to the non-equilibrium evaporative effect of local water which was originally from precipitation (Li et al., 2021). When compared to the corresponding LMWL, Kaseke et al. (2017) reported that advective fog had higher d due to remote vapor sources. For the radiation fog events in this study, the water vapor isotopic variability was mainly affected by local land-atmosphere interactions. However, the cold frontal clouds induced decreasing $\delta^2\text{H}_v$ in event 5, which was of similar amplitude as in previous studies (Aemisegger et al., 2015; Spiegel et al., 2012; Wen et al., 2008).

In our study, we found that radiation fog evolution, although driven by local land-atmosphere interaction, caused similar temporal variability in water vapor isotope amplitudes (events 1–4: 24.6‰ for $\delta^2\text{H}_v$ and 11.3‰ for d_v ; Table 1) as that induced by large-scale cold frontal passages (event 5; 34.6‰ for $\delta^2\text{H}_v$ and 9.3‰ for d_v ; Table 1). This reveals that water vapor isotope dynamics induced by processes controlling radiation fog evolution are as important in continental Europe as large-scale frontal passages. Isotopes can therefore likely provide invaluable constraints in addition to traditional meteorological measurements and modelling for improving the representation of fog dynamics in numerical weather prediction models.

5. Conclusions

Our event-based investigation of different radiation fog evolution cases and their stable water vapor isotope signature combined with meteorological and EC measurements highlight the relevance of different processes affecting the water budgets and evolution of radiation fog. We discussed the impact of dew and fog formation, fog droplet deposition, entrainment of air from the environment during fog growth, and evaporation of fog droplets after sunrise on the water vapor isotope signal in the near-surface atmosphere. Additionally, with the help of vertical profiles extracted from a high-resolution numerical weather prediction model analysis dataset (COSMO-1), the situation of fog lifting to stratus clouds could be interpreted. Fog identified using ground-level visibility measurements was found to occur only when the atmospheric air at standard height of 2 m a.g.l. was saturated. While shallow radiation fog dissipated at around sunrise, successful transition of radiation fog from shallow to deep fog allowed fog to persist for 3.5–4.0 h after sunrise in some cases. Fog lifting to stratus clouds caused immediate fog dissipation at ground level due to reduced surface longwave cooling and increased longwave warming by clouds.

During shallow radiation fog events dominated by equilibrium fractionation processes, the atmospheric water vapor showed a constant d_v at low values of the diel variability and linearly decreasing q_a and $\delta^2\text{H}_v$ mainly controlled by the rate of condensation. The transition of radiation fog from shallow to deep fog complicated the temporal variability of water vapor isotope signal mainly due to the combined influence of condensation, fog droplet deposition, the entrainment of air at fog-top, and the evaporation of fog droplets. The water vapor isotopic signal during the transition and deep radiation fog stages was characterized by a combination of condensation and mixing processes with negatively buoyant air bringing warmer air from the fog-top layer into the fog layer. The water vapor imported into the fog layer during this growth stage led to an increase in d_v while $\delta^2\text{H}_v$ depended on the

dominance of either condensation or entrainment. The temporal evolution in the $d_v-\delta^2H_v$ phase space thus provided useful insights into the relative importance of these two processes. After sunrise, the evaporation of fog droplets led to latent cooling. These negatively buoyant air parcels entrained water vapor formed from fog-top droplet evaporation into the fog layer, thereby mixing down water vapor enriched in heavy isotopes. Consequently, a substantial increase in δ^2H_v could be observed in our data during the fog dissipation period after sunrise.

Water vapor isotope dynamics associated with radiation fog evolution were found to induce variability of similar amplitude as the variability induced by large-scale cold frontal clouds. Our analysis showed that isotope measurements in the near-surface atmosphere combined with isotope-enabled modeling could provide invaluable additional constraints for achieving an improved representation of radiation fog dynamics in numerical models. To gain further insights into the radiation fog dynamics and lifetime, isotope observations in fog droplets, ambient water vapor from multiple vertical levels and from the deposited dew and fog droplets combined with high resolution isotope-enabled numerical modeling would be very valuable.

Author contributions

YL, FA, WE, and AR designed the project. FA carried out the instrument calibration in the laboratory. YL and WE performed the instrument installation at the field site. FA prepared the code of L2130-i data calibration and Rayleigh condensation model. SW prepared the code for downloading COSMO-1 data. YL processed and analyzed the data. FA, WE, and SW commented on the results of the data analysis. YL wrote and revised the manuscript, with contributions and feedback by FA, WE, SW, AR, and NB. WE passed away on 23 May 2022 during the review process of this study.

Declaration of Competing Interest

The authors declare that they have no competing financial interests or personal relationships that could have appeared to influence the work reported in this paper.

Data availability

Data are available from the ETH Zurich research collection at <https://doi.org/10.3929/ethz-b-000513287>.

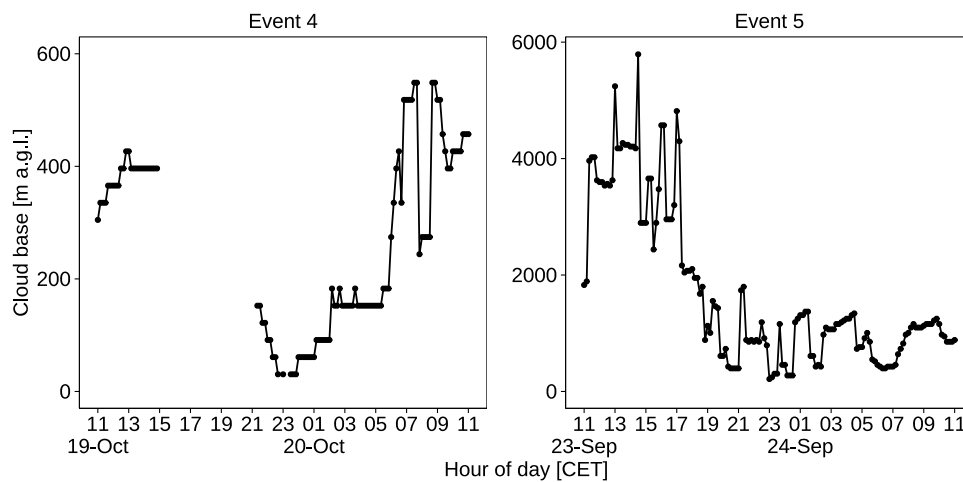


Fig. A1. Cloud base measured by a CL31 ceilometer (CL31, Vaisala, Bonn, Germany) at Nottwil, Switzerland which is 22 km in the southwest of CH-CHA site, during events 4 with fog lifting to stratus cloud, and event 5 with cold frontal clouds. The data was provided by Rega – Swiss Air-Rescue.

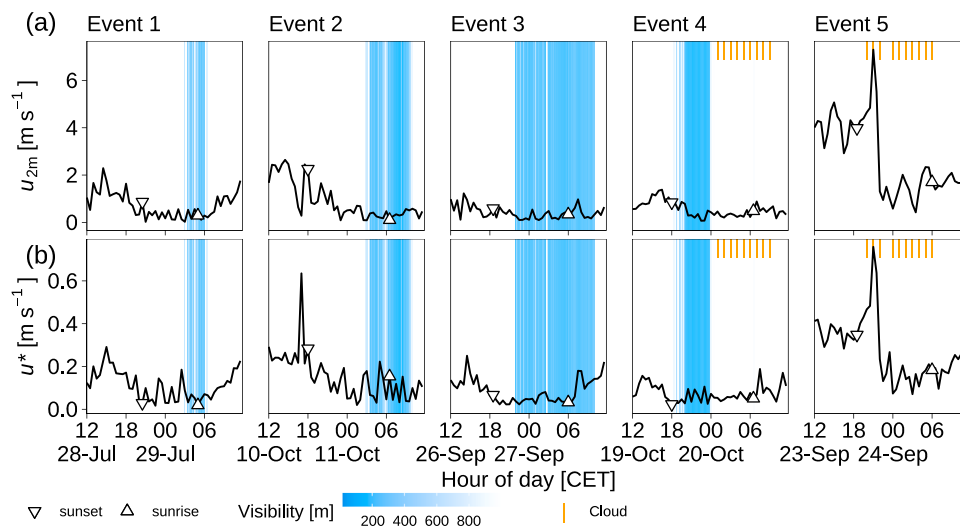


Fig. A2. Horizontal mean wind speed (u_{2m}) at 2 m a.g.l. and friction velocity (u^*) during the five events. During events 1–4, visibility < 1000 m (1-min averages) indicates fog occurrences; no fog occurred in event 5 with cloud frontal clouds. Cloud was interpreted using COSMO-1 analyses when the maximum values of liquid water content (LWC_{max}) in a vertical profile was higher than zero.

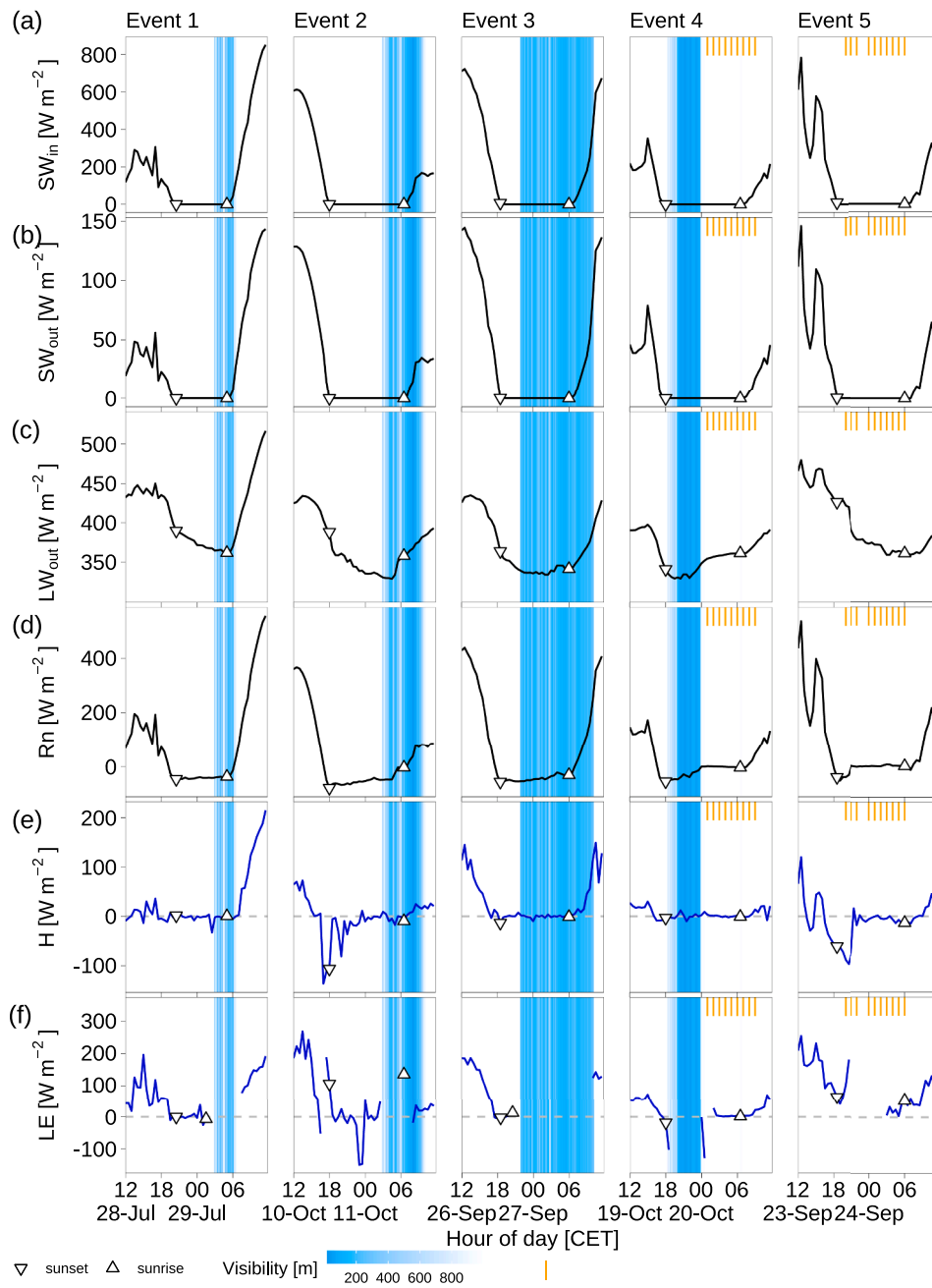


Fig. A3. Energy fluxes during the five events. (a) Short-wave incoming radiation (SW_{in}). (b) Short-wave outgoing radiation (SW_{out}). (c) Long-wave outgoing radiation. (d) Net radiation (R_n). (e) Turbulent sensible heat flux. (f) Turbulent latent heat flux. Fog occurs with visibility < 1000 m (1-min averages). Cloud coverage was extracted from COSMO-1 analyses when the maximum of LWC (LWC_{max}) in a liquid water path was non-zero; the cloud coverage extracted from the nearest grid cell of CH-CHA site is shown in orange; the cloud coverage extracted from the eight neighboring grid cells of CH-CHA site is shown in red. Cloud was interpreted using COSMO-1 analyses when the maximum values of liquid water content (LWC_{max}) in a vertical profile was higher than zero.

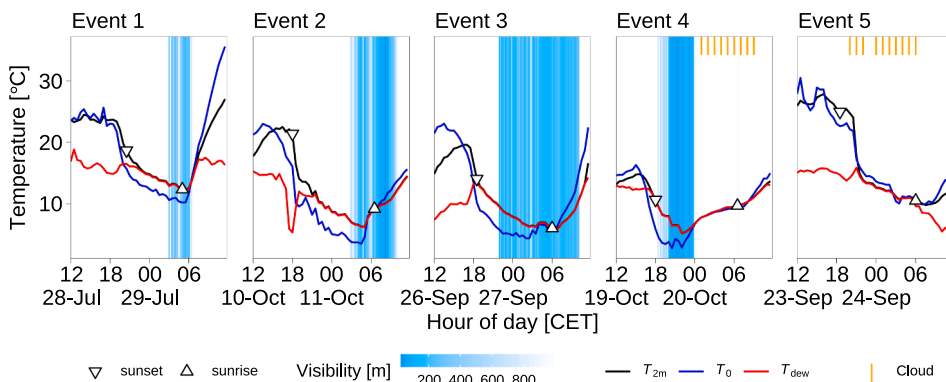


Fig. A4. Atmospheric temperature (T_{2m}) at 2 m a.g.l., surface temperature (T_0) computed from longwave radiation measurements, and dew-point temperature (T_{dew}). Fog occurs with visibility < 1000 m (1-min averages). Cloud presence was extracted from COSMO-1 analyses when the maximum of LWC (LWC_{max}) in a liquid water path was non-zero; the cloud coverage extracted from the nearest grid cell of CH-CHA site is shown in orange; the cloud coverage extracted from the eight neighboring grid cells of CH-CHA site is shown in red. Cloud was interpreted using COSMO-1 analyses when the maximum values of liquid water content (LWC_{max}) in a vertical profile was higher than zero.

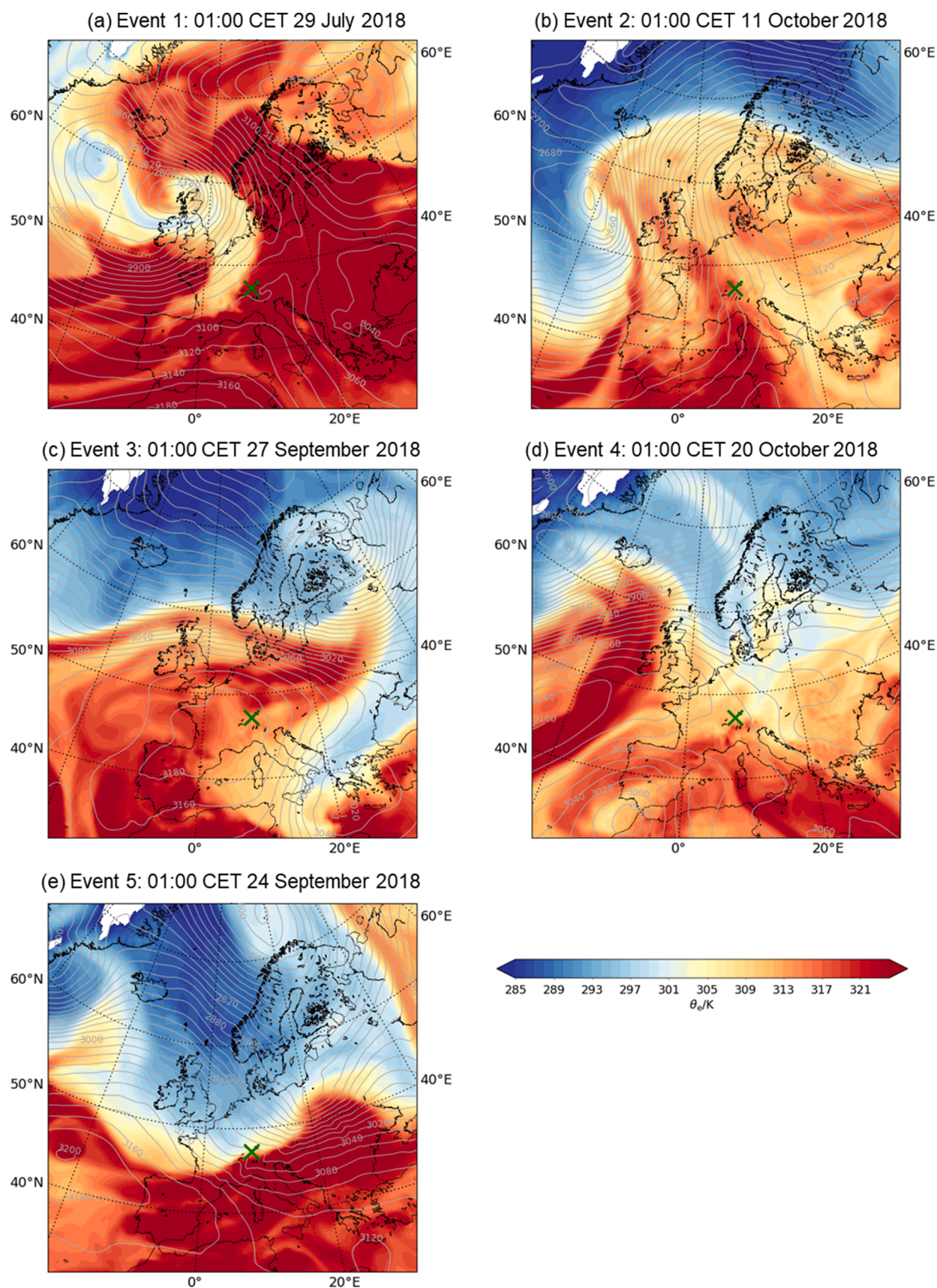


Fig. A5. Geopotential height (gray contours; m a.s.l.) and equivalent potential temperature (θ_e ; K) at 700 hPa at 01:00 CET during the five events extracted from ERA5 reanalysis data by European Centre for Medium-Range Weather Forecasts (ECMWF). The location of CH-CHA site is marked with green cross symbols.

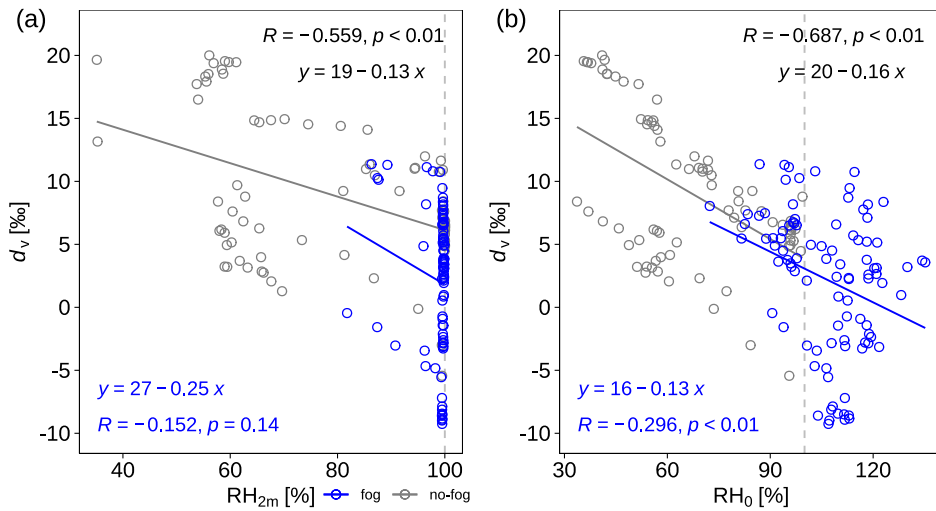


Fig. A6. Correlation between deuterium excess (d_v) of atmospheric water vapor with (a) atmospheric relative humidity (RH_{2m}) at 2 m a.g.l. and (b) surface relative humidity (RH_0). The data for fog periods are shown in blue, and no-fog periods are shown in black.

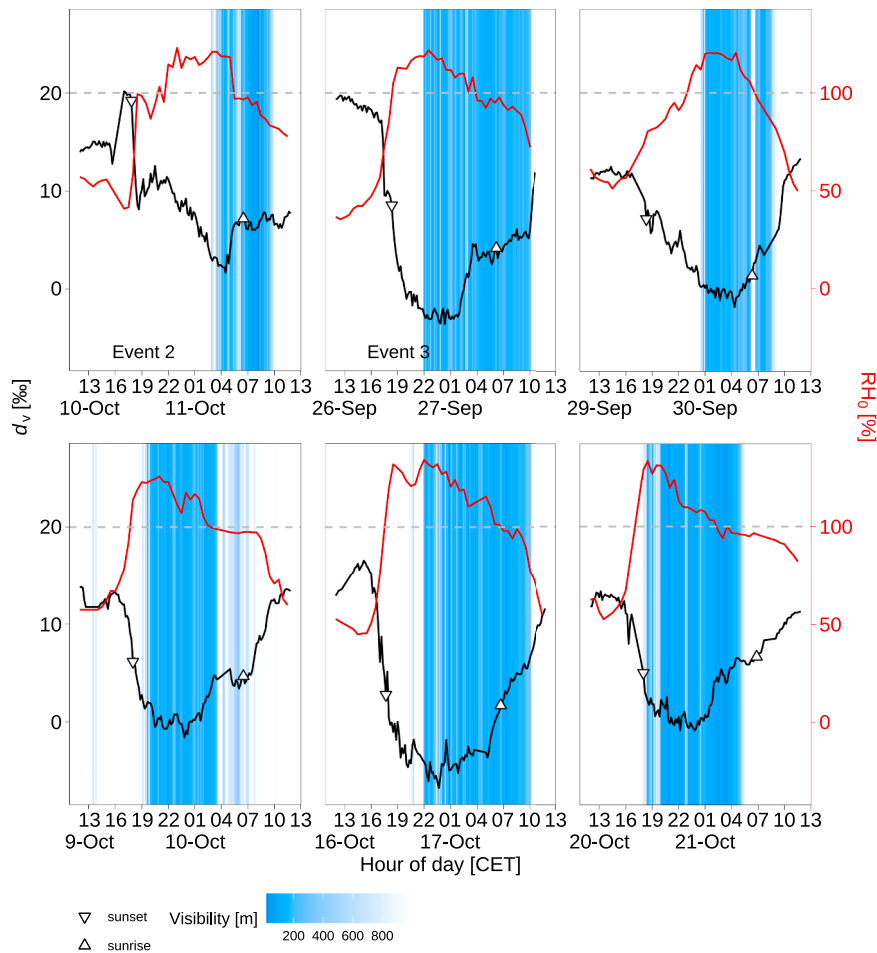


Fig. A7. Typical shallow radiation fog events occurring around sunrise at the CH-CHA site located on a valley bottom. Deuterium excess (d_v) of atmospheric water vapor is shown. Visibility < 1000 m indicates the occurrence of fog. Surface relative humidity (RH_0) was determined from surface temperature (T_0).

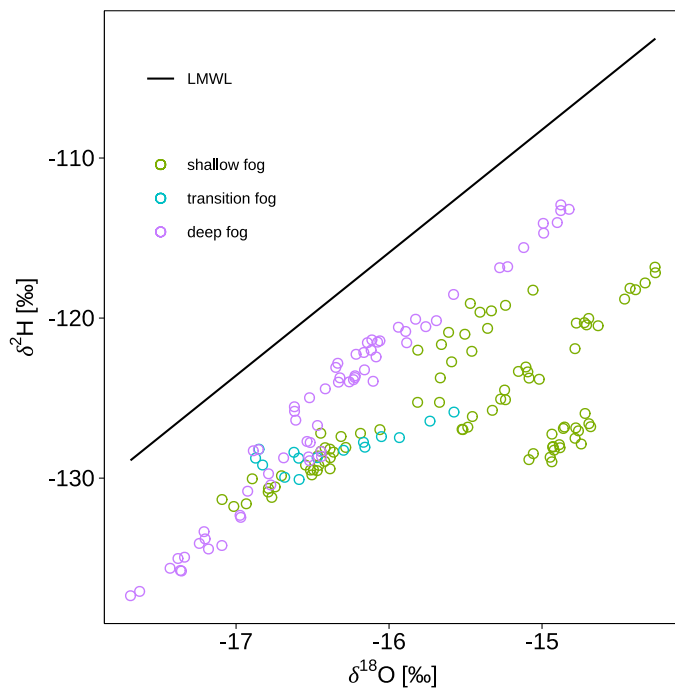


Fig. 8. The $\delta^2\text{H}$ – $\delta^{18}\text{O}$ pairs of near-surface atmospheric water vapor during fog periods (dots) in respect to local meteoric water line (LMWL; line) representing the $\delta^2\text{H}$ – $\delta^{18}\text{O}$ of precipitation at CH-CHA site (Prechsl et al., 2014).

Acknowledgements

This research has been supported by the Swiss National Science Foundation (grant no. 175733). The Picarro L2130-i analyzer was provided by the Atmospheric Dynamics group (Prof. Dr. Heini Wernli) at ETH Zurich. We thank Dr. Iris Feigenwinter and Dr. Lukas Hörtnagl (ETH Zurich) for the quality check of EC and meteorological data. The agricultural education and advice center (LBBZ) staff at Chamau are thanked for maintaining the agricultural management of the CH-CHA field site. The authors acknowledge MeteoSwiss and ECWMF for giving us access to the data of COSMO-1 and ERA5 reanalysis, and REGA for the cloud base data.

Appendices

References

- Aemisegger, F., Pfahl, S., Sodemann, H., Lehner, I., Seneviratne, S.I., Wernli, H., 2014. Deuterium excess as a proxy for continental moisture recycling and plant transpiration. *Atmospheric Chemistry and Physics* 14 (8), 4029–4054. <https://doi.org/10.5194/acp-14-4029-2014>.
- Aemisegger, F., Spiegel, J.K., Pfahl, S., Sodemann, H., Eugster, W., Wernli, H., 2015. Isotope meteorology of cold front passages: A case study combining observations and modeling. *Geophys Res Lett* 42 (13), 5652–5660. <https://doi.org/10.1002/2015GL063988>.
- Aemisegger, F., Sturm, P., Graf, P., Sodemann, H., Pfahl, S., Knohl, A., Wernli, H., 2012. Measuring variations of $\delta^{18}\text{O}$ and $\delta^2\text{H}$ in atmospheric water vapour using two commercial laser-based spectrometers: an instrument characterisation study. *Atmos. Meas. Tech.* 5 (7), 1491–1511. <https://doi.org/10.5194/amt-5-1491-2012>.
- Allan, R.P., Arias, P.A., Barlow, M., Cerezo-Mota, R., Cherchi, A., Gan, T., Gergis, J., Jiang, D., Khan, A., Mba, W.P., Rosenfeld, D., Tierney, J., Zolina, O., 2021. Water cycle changes, Climate Change 2021: The Physical science basis. Contribution of Working Group I to the sixth assessment report of the intergovernmental panel on climate change. The Intergovernmental Panel on Climate Change (IPCC). available at <https://www.ipcc.ch/report/ar6/wg1/> (last access 2 December 2021).
- Aubinet, M., Vesala, T., Papale, D., 2012. Eddy covariance: a practical guide to measurement and data analysis. Springer, Dordrecht, p. 438. <https://doi.org/10.1007/978-94-007-2351-1>.
- Beswick, K.M., Hargreaves, K.J., Gallagher, M.W., Choularton, T.W., Fowler, D., 1991. Size-resolved measurements of cloud droplet deposition velocity to a forest canopy using an eddy-correlation technique. *Quarterly Journal of the Royal Meteorological Society* 117 (499), 623–645. <https://doi.org/10.1002/qj.49711749910>.
- Boutle, I.A., Finnenkoetter, A., Lock, A.P., Wells, H., 2016. The London Model: forecasting fog at 333 m resolution. *Quarterly Journal of the Royal Meteorological Society* 142 (694), 360–371. <https://doi.org/10.1002/qj.2656>.
- Breil, M., Christner, E., Cauquoin, A., Werner, M., Karremann, M., Schädler, G., 2021. Applying an isotope-enabled regional climate model over the Greenland ice sheet: effect of spatial resolution on model bias. *Clim. Past* 17 (4), 1685–1699. <https://doi.org/10.5194/cp-17-1685-2021>.
- Brujinzeel, L., Eugster, W., Burkard, R., 2006. Fog as a hydrologic input, Encyclopedia of hydrological sciences. John Wiley & Sons, Ltd 1–24. <https://doi.org/10.1002/0470848944.hsa041>.
- Castillo-Botón, C., Casillas-Pérez, D., Casanova-Mateo, C., Ghimire, S., Cerro-Prada, E., Gutierrez, P.A., Deo, R.C., Salcedo-Sanz, S., 2022. Machine learning regression and classification methods for fog events prediction. *Atmospheric Research* 272, 106157. <https://doi.org/10.1016/j.atmosres.2022.106157>.
- Clark, I.D., Fritz, P., 1997. Environmental isotopes in hydrogeology. CRC Press, Boca Raton. <https://doi.org/10.1201/9781482242911>.
- Craig, H., Gordon, L.I., 1965. Deuterium and oxygen 18 variations in the ocean and the marine atmosphere, Stable isotopes in oceanographic studies and paleotemperatures. Consiglio nazionale delle ricerche, Laboratorio de geologia nucleare Pisa, Spoleto, Italy, pp. 9–130.
- Criss, R.E., 1999. Principles of stable isotope distribution. Oxford University Press, New York, Oxford. <https://doi.org/10.1093/oso/9780195117752.001.0001>.
- Dansgaard, W., 1964. Stable isotopes in precipitation. *Tellus* 16 (4), 436–468. <https://doi.org/10.1111/j.2153-3490.1964.tb00181.x>.
- Dawson, T.E., 1998. Fog in the California redwood forest: ecosystem inputs and use by plants. *Oecologia* 117 (4), 476–485. <https://doi.org/10.1007/s004420050683>.
- Delattre, H., Vallet-Coulomb, C., Sonzogni, C., 2015. Deuterium excess in the atmospheric water vapour of a Mediterranean coastal wetland: regional vs. local signatures. *Atmos. Chem. Phys.* 15 (17), 10167–10181. <https://doi.org/10.5194/acp-15-10167-2015>.
- Diekmann, C.J., Schneider, M., Ertl, B., Hase, F., García, O., Khosrawi, F., Sepúlveda, E., Knippertz, P., Braesicke, P., 2021. The global and multi-annual MUSICA IASI {H₂O, δD} pair dataset. *Earth Syst. Sci. Data* 13 (11), 5273–5292. <https://doi.org/10.5194/essd-13-5273-2021>.
- Dongmann, G., Nurnberg, H.W., Forstel, H., Wagener, K., 1974. On the enrichment of H₂O in the leaves of transpiring plants. *Radiation and Environmental Biophysics* 11 (1), 41–52. <https://doi.org/10.1007/BF01323099>.
- Eugster, W., 2008. Fog Research. *Erde* 139 (1–2), 1–10 available at: <http://homepage.usys.ethz.ch/eugsterw/publications/fog/index.html> (last access on 16 Feb 2022).
- Fischer, D.T., Still, C.J., Ebert, C.M., Baguskas, S.A., Williams, A.P., 2016. Fog drip maintains dry season ecological function in a California coastal pine forest. *Ecosphere* 7 (6). <https://doi.org/10.1002/ecs2.1364>.
- Garratt, J.R., 1992. The atmospheric boundary layer. Cambridge atmospheric and space science series. Cambridge University Press, Cambridge, England, p. 336.
- Gultepe, I., Tardif, R., Michaelides, S.C., Cermak, J., Bott, A., Bendix, J., Müller, M.D., Pagowski, M., Hansen, B., Ellrod, G., Jacobs, W., Toth, G., Cober, S.G., 2007. Fog research: A review of past achievements and future perspectives. *Pure Appl Geophys* 164 (6–7), 1121–1159. <https://doi.org/10.1007/s00024-007-0211-x>.
- Guo, L.J., Guo, X.L., Luan, T., Zhu, S.C., Lyu, K., 2021. Radiative effects of clouds and fog on long-lasting heavy fog events in northern China. *Atmospheric Research* 252. <https://doi.org/10.1016/j.atmosres.2020.105444>.
- Huang, L., Wen, X., 2014. Temporal variations of atmospheric water vapor δD and δ¹⁸O above an arid artificial oasis cropland in the Heihe River Basin. *Journal of Geophysical Research: Atmospheres* 119 (19), 476. <https://doi.org/10.1002/2014JD021891>, 11,456–11.
- IAEA, 2009. Reference sheet for VSMOW2 and SLAP2 international measurement standards. International Atomic Energy Agency (IAEA), Vienna, Austria, p. 8.
- Kaseke, K.F., Wang, L., 2022. Reconciling the isotope-based fog classification with meteorological conditions of different fog types. In: *J Hydrol*, 605, 127321. <https://doi.org/10.1016/j.jhydrol.2021.127321>.
- Kaseke, K.F., Wang, L.X., Seely, M.K., 2017. Nonrainfall water origins and formation mechanisms. *Sci. Adv.* 3 (3), e1603131 <https://doi.org/10.1126/sciadv.1603131>.
- Kidron, G.J., Starinsky, A., 2019. Measurements and ecological implications of non-rainfall water in desert ecosystems—A review. *Ecology* 12 (6). <https://doi.org/10.1002/eco.2121>.
- Lacour, J.L., Flamant, C., Risi, C., Clerbaux, C., Coheur, P.F., 2017. Importance of the Saharan heat low in controlling the North Atlantic free tropospheric humidity budget deduced from IASI δD observations. *Atmos. Chem. Phys.* 17 (15), 9645–9663. <https://doi.org/10.5194/acp-17-9645-2017>.
- LaDochy, S., Witwi, M.R., 2013. Fog Hazard Mitigation. Editor. In: Bobrowsky, P.T. (Ed.), *Encyclopedia of Natural Hazards*. Springer Netherlands, Dordrecht, pp. 338–342. https://doi.org/10.1007/978-1-4020-4399-4_350.
- Li, Y., Aemisegger, F., Riedl, A., Buchmann, N., Eugster, W., 2021. The role of dew and radiation fog inputs in the local water cycling of a temperate grassland during dry spells in central Europe. *Hydrol. Earth Syst. Sci.* 25 (5), 2617–2648. <https://doi.org/10.5194/hess-25-2617-2021>.
- LI-COR, 2019. Eddy covariance processing software (Version 7.0.6) [Software]. LI-COR. LI-COR, Inc. https://www.licor.com/env/products/eddy_covariance/software.html.
- López, A., Molina-Aiz, F.D., Valera, D.L., Peña, A., 2012. Determining the emissivity of the leaves of nine horticultural crops by means of infrared thermography. *Scientia Horticulturae* 137, 49–58. <https://doi.org/10.1016/j.scienta.2012.01.022>.
- Majoube, M., 1971. Fractionnement en oxygène 18 et en deutérium entre l'eau et sa vapeur. *J. Chim. Phys.* 68, 1423–1436. <https://doi.org/10.1051/jcp/1971681423>.

- Mazoyer, M., Lac, C., Thouron, O., Bergot, T., Masson, V., Musson-Genon, L., 2017. Large eddy simulation of radiation fog: impact of dynamics on the fog life cycle. *Atmos. Chem. Phys.* 17 (21), 13017–13035. <https://doi.org/10.5194/acp-17-13017-2017>.
- Merlivat, L., Jouzel, J., 1979. Global climatic interpretation of the deuterium-oxygen 18 relationship for precipitation. *Journal of Geophysical Research: Oceans* 84 (C8), 5029–5033. <https://doi.org/10.1029/JC084iC08p05029>.
- Moene, A.F., van Dam, J.C., 2014. *Transport in the Atmosphere-Vegetation-Soil Continuum*. Cambridge University Press, Cambridge. <https://doi.org/10.1017/CBO9781139043137>.
- Müller, M.D., Masbou, M., Bott, A., 2010. Three-dimensional fog forecasting in complex terrain. *Quarterly Journal of the Royal Meteorological Society* 136 (653), 2189–2202. <https://doi.org/10.1002/qj.705>.
- Noone, D., 2012. Pairing measurements of the water vapor isotope ratio with humidity to deduce atmospheric moistening and dehydration in the tropical midtroposphere. *J Climate* 25 (13), 4476–4494. <https://doi.org/10.1175/JCLI-D-11-00582.1>.
- Parkes, S.D., McCabe, M.F., Griffiths, A.D., Wang, L., Chambers, S., Ershadi, A., Williams, A.G., Strauss, J., Element, A., 2017. Response of water vapour D-excess to land-atmosphere interactions in a semi-arid environment. *Hydrology and Earth System Sciences* 21 (1), 533–548. <https://doi.org/10.5194/hess-21-533-2017>.
- Philip, A., Bergot, T., Bouteloup, Y., Bouysse, F., 2016. The Impact of Vertical Resolution on Fog Forecasting in the Kilometeric-Scale Model AROME: A Case Study and Statistics. *Weather Forecast* 31 (5), 1655–1671. <https://doi.org/10.1175/WAF-D-16-0074.1>.
- Pithani, P., Ghude, S.D., Chennu, V.N., Kulkarni, R.G., Steeneveld, G.-J., Sharma, A., Prabhakaran, T., Chate, D.M., Gulpe, I., Jenamani, R.K., Madhavan, R., 2019. WRF Model Prediction of a Dense Fog Event Occurred During the Winter Fog Experiment (WIFEX). *Pure Appl Geophys* 176 (4), 1827–1846. <https://doi.org/10.1007/s00024-018-2053-0>.
- Prechsl, U.E., Gilgen, A.K., Kahmen, A., Buchmann, N., 2014. Reliability and quality of water isotope data collected with a lowbudget rain collector. *Rapid Communications in Mass Spectrometry* 28 (8), 879–885. <https://doi.org/10.1002/rcm.6852>.
- Price, J., 2011. Radiation fog. Part I: Observations of stability and drop size distributions. *Bound-Lay Meteorol* 139 (2), 167–191. <https://doi.org/10.1007/s10546-010-9580-2>.
- Price, J.D., Clark, R., 2014. On the Measurement of Dewfall and Fog-Droplet Deposition. *Bound-Lay Meteorol* 152 (3), 367–393. <https://doi.org/10.1007/s10546-014-9930-6>.
- Price, J.D., Lane, S., Boutle, I.A., Smith, D.K.E., Bergot, T., Lac, C., Duconge, L., McGregor, J., Kerr-Munslow, A., Pickering, M., Clark, R., 2018. LANFEX: A Field and Modeling Study to Improve Our Understanding and Forecasting of Radiation Fog. *B Am Meteorol Soc* 99 (10), 2061–2077. <https://doi.org/10.1175/BAMS-D-16-0299.1>.
- Román-Cascón, C., Yagüe, C., Steeneveld, G.-J., Morales, G., Arrillaga, J.A., Sastre, M., Maqueda, G., 2019. Radiation and cloud-base lowering fog events: Observational analysis and evaluation of WRF and HARMONIE. *Atmospheric Research* 229, 190–207. <https://doi.org/10.1016/j.atmosres.2019.06.018>.
- Schneider, M., Ertl, B., Diekmann, C.J., Khosrawi, F., Weber, A., Hase, F., Höpfner, M., García, O.E., Sepúlveda, E., Kinnison, D., 2022. Design and description of the MUSICA IASI full retrieval product. *Earth Syst. Sci. Data* 14 (2), 709–742. <https://doi.org/10.5194/essd-14-709-2022>.
- Scholl, M., Eugster, W., Burkard, R., 2011. Understanding the role of fog in forest hydrology: stable isotopes as tools for determining input and partitioning of cloud water in montane forests. *Hydrological Processes* 25 (3), 353–366. <https://doi.org/10.1002/hyp.7762>.
- Schraff, C., Hess, R., 2012. A description of the nonhydrostatic regional COSMOmodel, Part III: Data assimilation. COSMO Documentation. http://www.cosmo-model.org/content/model/documentation/core/cosmo_physics_4.20.pdf.
- Smith, D.K.E., Renfrew, I.A., Price, J.D., Dorling, S.R., 2018. Numerical modelling of the evolution of the boundary layer during a radiation fog event. *Weather* 73 (10), 310–+. <https://doi.org/10.1002/wea.3305>.
- Spiegel, J.K., Aemisegger, F., Scholl, M., Wienhold, F.G., Collett, J.L., Lee, T., van Pinxteren, D., Mertes, S., Tilgner, A., Herrmann, H., Werner, R.A., Buchmann, N., Eugster, W., 2012. Temporal evolution of stable water isotopologues in cloud droplets in a hill cap cloud in central Europe (HCCT-2010). *Atmospheric Chemistry and Physics* 12 (23), 11679–11694. <https://doi.org/10.5194/acp-12-11679-2012>.
- Stull, R.B., 1988. Stable boundary layer. Editor. In: Stull, R.B. (Ed.), *An Introduction to Boundary Layer Meteorology*. Springer, Dordrecht, Dordrecht, pp. 499–543. https://doi.org/10.1007/978-94-009-3027-8_12.
- Tada, M., Yoshimura, K., Toride, K., 2021. Improving weather forecasting by assimilation of water vapor isotopes. *Sci Rep-Uk* 11 (1), 18067. <https://doi.org/10.1038/s41598-021-97476-0>.
- Thurnherr, I., Aemisegger, F., 2022. Disentangling the impact of air-sea interaction and boundary layer cloud formation on stable water isotope signals in the warm sector of a Southern Ocean cyclone. *Atmos. Chem. Phys. Discuss.* 2022, 1–31. <https://doi.org/10.5194/acp-2022-12>.
- Thurnherr, I., Hartmuth, K., Jansing, L., Gehring, J., Boettcher, M., Gorodetskaya, I., Werner, M., Wernli, H., Aemisegger, F., 2021. The role of air-sea fluxes for the water vapour isotope signals in the cold and warm sectors of extratropical cyclones over the Southern Ocean. *Weather Clim. Dynam.* 2 (2), 331–357. <https://doi.org/10.5194/wcd-2-331-2021>.
- Toride, K., Yoshimura, K., Tada, M., Diekmann, C., Ertl, B., Khosrawi, F., Schneider, M., 2021. Potential of Mid-tropospheric Water Vapor Isotopes to Improve Large-Scale Circulation and Weather Predictability. *Geophys Res Lett* 48 (5), e2020GL091698. <https://doi.org/10.1029/2020GL091698>.
- Urey, H.C., 1947. The thermodynamic properties of isotopic substances. *J Chem Soc* 562–581. <https://doi.org/10.1039/jr9470000562>.
- Waersted, E.G., Haefelin, M., Dupont, J.C., Delanoe, J., Dubuisson, P., 2017. Radiation in fog: quantification of the impact on fog liquid water based on ground-based remote sensing. *Atmospheric Chemistry and Physics* 17 (17), 10811–10835. <https://doi.org/10.5194/acp-17-10811-2017>.
- Wen, X.F., Sun, X.M., Zhang, S.C., Yu, G.R., Sargent, S.D., Lee, X., 2008. Continuous measurement of water vapor D/H and O-18/O-16 isotope ratios in the atmosphere. *J Hydrol* 349 (3–4), 489–500. <https://doi.org/10.1016/j.jhydrol.2007.11.021>.
- Westerhuis, S., 2020. Improving forecasts of fog and low stratus in a high-resolution numerical weather prediction model. Diploma thesis. ETH Zurich. <https://doi.org/10.3929/ethz-b-000469744>.
- Westerhuis, S., Fuhrer, O., Cermak, J., Eugster, W., 2020. Identifying the key challenges for fog and low stratus forecasting in complex terrain. *Quarterly Journal of the Royal Meteorological Society* 146 (732), 3347–3367. <https://doi.org/10.1002/qj.3849>.
- White, J.W.C., Gedzelman, S.D., 1984. The isotopic composition of atmospheric water-vapor and the concurrent meteorological conditions. *Journal of Geophysical Research-Atmospheres* 89 (Nd3), 4937–4939. <https://doi.org/10.1029/JD089iD03p04937>.